Plasma Sources Science and Technology

Global model of an atmospheric-pressure capacitive discharge in helium with air impurities from 100 to 10000 ppm

To cite this article before publication: Bowen Sun *et al* 2018 *Plasma Sources Sci. Technol.* in press https://doi.org/10.1088/1361-6595/aaf8e1

Global model of an atmospheric-pressure capacitive discharge in helium with air impurities from 100 to 10000 ppm

Bowen Sun[1], Dingxin Liu[1*], Felipe Iza[2], Sui Wang[1], Aijun Yang[1], Zhijie Liu[1], Mingzhe Rong[1] and Xiaohua Wang[1*]

[1] State Key Laboratory of Electrical Insulation and Power Equipment, Centre for Plasma Biomedicine, Xi'an Jiaotong University, 710049, P. R. China
[2] School of Mechanical, Electrical and Manufacturing Engineering, Loughborough University, LE11 3TU, UK

Email: liudingxin@mail.xjtu.edu.cn and xhw@mail.xjtu.edu.cn

Abstract

Helium is a common working gas for cold atmospheric plasmas (CAPs) and this is often mixed with other gases, such as oxygen and nitrogen, to increase its reactivity. Air is often found in these plasmas and it can be either introduced deliberately as a precursor or entrapped in systems that operate in open atmosphere. In either case, the presence of small traces of air can cause a profound change on the composition of the plasma and consequently its application efficacy. In this paper, a global model for He+Air CAPs is developed, in which 59 species and 866 volume reactions are incorporated, and a new boundary condition is used for the mass transport at the interface between the plasma and its surrounding air gas. The densities of reactive species and the power dissipation characteristics are obtained as a function of air concentrations spanning from 100 to 10000 ppm. As the air concentration increases, the dominant cation changes from O_2^+ to NO^+ and then to NO_2^+, the dominant anion changes from O_2^- to NO_2^- and then to NO_3^-, the dominant ground state reactive oxygen species changes from O to O_3, and the dominant ground state reactive nitrogen species changes from NO to HNO_2. O_2(a) is the most abundant metastable species and its density is orders of magnitude larger than other metastable species for all air concentrations considered in the study. Ion Joule heating is found important due to the electronegative nature of the plasma, which leads to the fast decrease of electron density when the air concentration is larger than 1000 ppm. The generation and loss pathways of important biologically relevant reactive species such as O, O_2^-, O_3, OH, H_2O_2, NO, HNO_2, HNO_3 are discussed and differences with the pathways observed in He+O_2, He+H_2O, Ar+Air and pure air plasmas are highlighted. Based on the simulation results, a simplified chemistry set with 47 species and 109 volume reactions is proposed. This simplified model greatly reduces the computational load while maintaining the accuracy of the simulation results within a factor of 2. The simplified chemistry model is computationally much less intensive, facilitating its integration into multidimensional fluid models for the study of the spatio-temporal evolution of He+Air CAPs.

1. Introduction

Cold atmospheric plasmas (CAPs) have found use in a wide range of applications such as environmental protection[1], surface modification[2] and biomedicine[3-5]. Helium is a commonly used as working gas for CAPs due to its good thermal conductivity and discharge stability. However, industrial helium normally has a purity level lower than 99.99% and as a result, traces of additional gases such as N_2 and O_2 are typically present in concentrations larger than 100 parts per million (ppm). Moreover, in many atmospheric-pressure applications helium plasmas are operated in open air and therefore air inevitably mixes into the helium working gas[6,7]. Given the large energy of helium and helium dimer metastables, Penning ionization is an important process in these discharges and even traces of gases in the ppm range can have a significant effect on the discharge properties and composition[8].

On one hand, the presence of air in helium plasmas is critical for the production of reactive oxygen species (ROS) and reactive nitrogen species (RNS), which are useful for various applications but on the other hand, the presence of air traces can compromise the plasma stability. Some recent reports have witnessed that gas impurities in the ppm range could dramatically change the plasma characteristics[9-12], maximize the production efficiency of ROS and/or RNS[13], when the concentration of traces are increased to several thousand ppm and cause instabilities of CAPs at higher concentration[14,15]. Therefore, helium CAPs are normally operated with admixtures of gases (typically air) in a concentration range of 100 to 10000 ppm, a regime where the plasma characteristics as well as the production of reactive species are significantly influenced by the actual background gas composition.

Quantifying the impact of the presence of air in the helium CAPs is of importance, both at a fundamental level, where the production mechanisms of ROS and RNS are not yet fully understood, and technologically, as the production efficiency of ROS and RNS needs to be optimized for different applications.

The chemistry in air-containing CAPs is so complex that quantitative studies have proved to be very challenging. At least dozens of species and hundreds of reactions need to be considered in these plasmas but only a few of the species can be measured with current diagnostic techniques[16]. Complimenting experiments, plasma modeling can provide insights into the chemistry of CAPs. Previous studies have used computational fluid models with simplified chemistry sets[17,18] without a rigorous approach for the simplification of the chemistry set or analysis of its accuracy. Global models have been widely used to study the chemistry of CAPs, as they provide a computationally effective way of study of complex plasma chemistry sets as those generated in air containing CAPs. Global models have already been successfully used to study CAPs with complex chemistry such as Ar+humid air[19], $He+O_2$ with humid air impurities[20], $Ar+H_2O$[21] and $He+O_2+H_2O$[22]. For He+Air plasmas, global model can provide insights into the different power dissipation channels, species densities, key species and chemical pathways. It is noted that the key species and reactions extracted from global models can then be used in fluid models for the study of plasma space variations[23,24], from which additional insights can be obtained.

In this paper, a global model is developed to study He+Air CAPs with air concentrations spanning from 100 to 10000 ppm. Following a comprehensive literature review, 59 chemical species and 866 volume reactions are incorporated in the model. The density of reactive species and the power dissipation of various physiochemical processes are discussed in detail as a function of the air concentration in the background gas. Due to their application relevance, special attention is paid on the chemical pathways of ROS and RNS. Careful analysis of the simulation results, allow us to identify the main species and reactions to create a simplified chemistry model. This model incorporates 47 species and 109 volume reactions, ~12% of the chemical reactions in the original model. The accuracy of the simplified model is assessed by comparing selected reactive species simulation results of the simplified model against those of the original model. Our goal is to explain the plasma chemistry of He+Air CAPs and develop a simplified chemistry set for incorporation in more elaborate fluid models in future study.

The paper is structured as follows. The description of the global model is given in section 2. Simulation results of the full global model are presented in section 3, where the densities of reactive species and power dissipations are discussed as a function of the air concentration in the feed gas. In section 4, simulation results of the simplified model are presented, where the accuracy and robustness are discussed, and the main pathways for the generation/loss of selected reactive species are illustrated. Finally, concluding remarks are given in section 5.

2. Global model

The global model used in this work is similar to that recently reported and used for the study of $Ar+H_2O$ plasmas [25]. Therefore, only the main differences between the two models are described here. Emphasis is made on the new species and chemical reactions, which are significantly different to those in $Ar+H_2O$ plasmas, as well as the improved modeling of the radial loss of neutral species.

Figure 1 shows a schematic diagram of the He+Air plasma system considered in this study. It consists of two parallel circular plates with radius R = 1 cm, with a gap between the two of g = 2 mm. The plasma is excited with an average power density of 10 W/cm^3, the neutral gas temperature is set to remain at room temperature (300 K), and the gas flow rate is set to be 100 standard cubic centimeter per minute (sccm). The air concentration in the

He+Air feedstock gas is varied from 100 ppm to 10000 ppm, and the air is assumed to have a composition of 79% N_2, 20% O_2 and 1% H_2O (1% H_2O corresponds to a relative humidity of approximately 30% at 300 K and 1 atmosphere, which is a typical inland air humidity) [26,27].

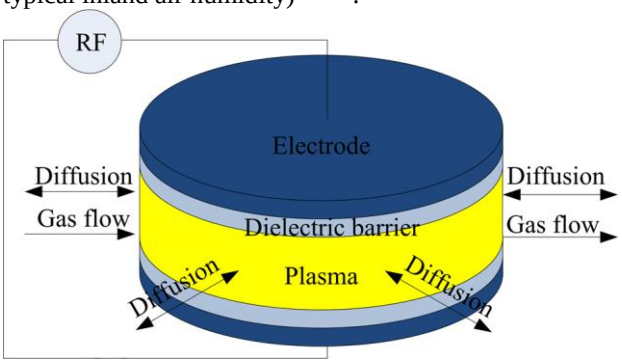

Figure 1. Schematic diagram of the model

The model incorporates 59 species and 866 volume reactions, in which 53 species and 624 reactions are identical to a comprehensive model for air plasmas previously reported by Sakiyama *et al*[26]. The additional 6 species and 242 volume reactions are all helium-related, which have been identified after an extensive literature review. The incorporated helium species are He, He^*, He_2^*, He^+, He_2^+ and HeH^+, and the helium-related reactions are listed in the Appendix I. Since we are mainly interested in the biomedical application of these plasmas, the paper focuses on biologically relevant reactive components. Hydrated species often encountered in high humidity plasmas and high order clusters such as O_6^+ are assumed to be negligible for the conditions of this study. The total species, including cations, anions, metastables and ground-state neutrals are listed in table 1. Most rate coefficients are taken from literature and where possible electron collision reaction coefficients are calculated based on cross section data using BOLSIG+[28]. When both rate coefficients and cross section data are not available, rates have been estimated according to the recommendations by Kushner and Kossyi *et al*. [29,53].

Table 1. Species included in this model

Type	Species
Positive charge species	He^+, He_2^+, HeH^+, N^+, N_2^+, N_3^+, N_4^+, O^+, O_2^+, O_4^+, NO^+, N_2O^+, NO_2^+, H^+, H_2^+, H_3^+, OH^+, H_2O^+, H_3O^+
Negative charge species	e, O^-, O_2^-, O_3^-, O_4^-, NO^-, N_2O^-, NO_2^-, NO_3^-, H^-, OH^-
Metastables	He^*, He_2^*, $N(^2D)$, $N_2(A)$, $N_2(B)$, $O(^1D)$, $O_2(a)$
Grounded neutrals	He,H, N, O, O_3, NO, N_2O, NO_2, NO_3, N_2O_3, N_2O_4, N_2O_5, H_2, OH, HO_2, H_2O_2, HNO, HNO_2, HNO_3, N_2, O_2, H_2O

The particle balance equation for each plasma species is given by[10]:

$$\frac{dn_k}{dt} = G_k^V + \frac{S_1}{V}\left(\sum_{i=1,i\neq k}^{N} \alpha_{i,k}\Gamma_{1i} - \beta_k\Gamma_{1k}\right) - \frac{S_2}{V}\Gamma_{2k} - \frac{F}{V}n_k \quad (1)$$

where n_k is the number density of species k, G_k^V is the net generation/loss rate of species k due to volume reactions in the plasma, N is the total number of species, S_1 is the total area of the solid plates, S_2 is the "sidewall" area of the plasma-gas interface, V is the plasma volume, Γ_{1k} is the flux of species k to the solid plates, Γ_{2k} is the flux of species k to the sides out of the plasma, and F is the gas flow rate.

The second term on the right-hand side of equation 1 represents the particle gain/loss due to surface reactions, in which β_k is the surface reaction probability of species k, and $\alpha_{i,k}$ is a parameter between zero and one that relates to the generation probability of species k due to surface reactions of species i. All the cations are assumed to be neutralized when reaching the dielectric barriers and therefore β_k=1 for them. Anions are assumed to be confined in the plasma region by the ambipolar field and therefore $\beta_k\Gamma_{1k}$=0[31,32]. Due to the collisionality of the sheaths, the flux of cations is calculated using the following formula[25]

$$\Gamma_{1k} = \frac{0.6 n_k u_B}{\sqrt{1+\frac{\pi\lambda_{Ds}}{2\lambda_{ion}}}} \quad (2)$$

where u_B represents the Bohm velocity, λ_{Ds} is the Debye length in the plasma sheath, λ_{ion} is the mean free path of positive ions. Finally, the electron flux is set to balance the total flux of cations, maintaining quasi-neutrality in the bulk plasma.

Reactive neutral species are assumed to be absorbed by the dielectric barriers with the value of β_k varies between zero and one[9]. The axial diffusive loss of a reactive species is calculated using the following formula[31]

$$\beta_k\Gamma_{1k} = k_z^2 D_k n_k g \quad (3)$$

with

$$k_z^2 = \left(\frac{g^2}{12} + \frac{D_k g}{v_k}\frac{2-\beta_k}{\beta_k}\right)^{-1} \quad (4)$$

where g is the gap length, D_k is the diffusion coefficient of species k, which is calculated following the approach described in ref. [30]. v_k is the thermal mean speed of species k. For the derivation of the formulas (2)-(4), please refer to Ref. [25] and [31].

The third term on the right-hand side of equation 1 represents the particle gain/loss due to sidewise diffusion. The sidewise gain and loss are estimated for the neutral species as reported in ref. [31] and [32]. Since only a small proportion of the helium gas is transformed into other species (such as helium metastables), the helium concentration in the feedstock gas is assumed to remain constant in the plasma. However, this is not the case for air species as a large portion of the N_2, O_2 and H_2O molecules are dissociated and/or ionized in the discharge. As a result, the three species (N_2, O_2 and H_2O) diffuse from the

surrounding gas into the plasma region, where they are consumed. Following a similar derivation to that in ref. [31], it can be shown that the sidewise flux (Γ_{2k}) for N_2, O_2 and H_2O at the radial boundary is given by:

$$\Gamma_{2k} = \frac{2D_k}{R}\left(1-\frac{n_{k,ext}^2}{n_k^2}\right)n_k \qquad (5)$$

where k represents N_2, O_2 and H_2O, $n_{k,ext}$ represents the number density of species k in the surrounding (feed) gas, n_k the average density of species k in the plasma region, D_k is the diffusion coefficient of species k. It is noted that equation (5) given in ref. [31] is just for water, but it should also be applied to N_2 and O_2 in He+Air plasmas.

The model also accounts for neutral species were not present in the background gas but are generated in the plasma. These species diffuse outwards and Appendix II details the derivation of an expression for the flux Γ_{2k} of these species at the radial boundary of the discharge region [32]. This flux is given by:

$$\Gamma_{2k} = \frac{1}{4}n_k \frac{R^2\sqrt{D_k K}\sum_{m=1}\frac{2m\left(\sqrt{\frac{K}{D_k}}R\right)^{2m-1}}{2^{2m}(m!)^2}}{\int_0^R 2r\left(\sqrt{D_k K}\sum_{m=1}\frac{2m\left(\sqrt{\frac{K}{D_k}}R\right)^{2m-1}}{2^{2m}(m!)^2}+0.25I_0\left(\sqrt{\frac{K}{D_k}}R\right)v_{th}-0.25v_{th}I_0\left(\sqrt{\frac{K}{D_k}}r\right)\right)dr}v_{th,k} \qquad (6)$$

where n_k represents the average density of species k across the radial direction, D_k represents the diffusion coefficient and K represents the reaction frequency for the destruction (linear approximation) of species k. $v_{th,k}$ is the mean thermal velocity, I_0 represents the modified zero-order Bessel function of the first kind. K changes in time as the plasma composition evolves. To account for this time evolution, K is evaluated and updated at each time step in the simulation.

For long-lived species, K is small enough for the loss of species at the boundary to contribute significantly to the loss of particles, and consequently the density at the radial plasma boundary ($n(R)$) is expected to be much lower than the average density in the discharge (n_{ave}).

On the other hand, short-lived species are readily lost and therefore the contribution of the radial diffusion out of the plasma region on the lifetime of these species is small. As a result, the radial profile of the density of these species is relatively uniform across the discharge region and the density at the radial boundary of the plasma ($n(R)$) is approximately equal to the average density (n_{ave}) in the plasma.

In general, the ratio of the density at the radial boundary to the average density in the discharge ($n(R)/n_{ave}$) is a function of K. As an example, Figure 2 shows this ratio for atomic oxygen as a function of K, when the diffusion coefficient of O is assumed to be 1×10^{-4} m^2/s. The ratio is calculated using the formula (A11) in Appendix II. The sidewise boundary loss rate ($S_{d,i}$) is given by $\Gamma_{2k}S_2/V$, where Γ_{2k} is calculated according to equation (6). The loss rate due to chemical reactions is given by Kn_{ave} and K is assumed to varied between 10^{-2} to 10^5 for the purposes of Figure 2.

As the value of K changes due to the time evolution of the plasma composition, the ratio $n(R)/n_{ave}$ and the radial loss contribution change by orders of magnitude. At low K values (K<10 s^{-1}) the ratio $n(R)/n_{ave}$ is around 2×10^{-4} and this increase linearly for K values above 10 s^{-1}. Correspondingly, the sidewise loss contributes nearly 100% of the loss of atomic oxygen when K<1 s^{-1} and this contribution decreases linearly for larger K values, being only 0.6% when K=10^5 s^{-1}. For the steady state conditions encountered in the plasmas investigated in this study, the K value for atomic oxygen is found to be on the order of 10^3 s^{-1}. For very short-lived species such as O(^{1}D), K is larger than 10^6 s^{-1} and for these species the sidewise loss can be neglected.

Table 2 shows the steady state values of K and the contribution of the sidewise loss to the total loss of the neutral species for the case of an air concentration of 10000 ppm. For short-lived species the sidewise loss accounts for less than 1% of the total loss and hence the sidewise loss can be neglected for these species without significantly affecting the simulation results. On the other hand, the radial loss can account for more than a quarter of the total losses for long lived species.

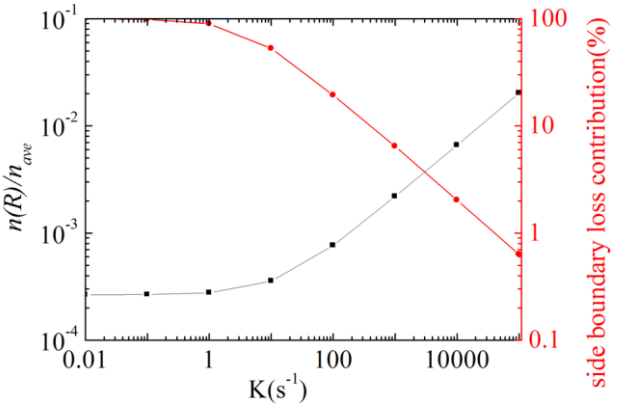

Figure 2. $n(R)/n_{ave}$ and side boundary loss contribution as a

function of K for O atoms(—■—: $n(R)/n_{ave}$; —●—: side boundary loss contribution($S_{d,i}/(S_{d,i}+Kn_{ave})$))

Table 2. Ratio of sidewise loss rate to total loss rate of species for the air impurity of 10000 ppm

Species	K	Sidewise loss contribution
$N(^2D)$	2.57×10^{5}	0.23%
$N_2(A)$	1.45×10^{5}	0.36%
$N_2(B)$	1.98×10^{7}	<0.01%
$O(^1D)$	9.32×10^{6}	<0.01%
H	1.01×10^{5}	1.00%
N	7.42×10^{3}	2.18%
O	2.61×10^{3}	4.04%
NO	2.97×10^{3}	3.03%
NO_2	1.18×10^{4}	1.52%
NO_3	2.40×10^{4}	0.97%
N_2O_3	4.34×10^{5}	0.10%
N_2O_4	1.99×10^{5}	0.18%
OH	1.79×10^{4}	1.50%
HO_2	1.61×10^{4}	1.35%
HNO	5.27×10^{4}	0.74%
He^*	4.18×10^{7}	<0.01%
He_2^*	1.98×10^{7}	<0.01%
O_3	8.40×10^{1}	15.88%
$O_2(a)$	5.40×10^{1}	22.10%
H_2	1.20×10^{1}	58.32%
H_2O_2	1.80×10^{1}	35.80%
N_2O	7.94×10^{2}	5.47%
N_2O_5	1.13×10^{2}	10.75%
HNO_2	4.50×10^{1}	20.50%
HNO_3	5.54×10^{2}	5.88%

Solution of the balance equation requires knowledge on the electron temperature (T_e) and this is calculated by solving the electron energy balance equation: [33]

$$\frac{d}{dt}\left(\frac{3}{2}n_eT_e\right)=\xi\left(\frac{P_{in}}{eV}-\frac{S_1}{V}\left(\varepsilon_e\Gamma_e+\sum_{j=1}^{N_p}\varepsilon_p\Gamma_{1j}\right)\right)-\sum_{i=1}^{N_r}\varepsilon_iR_i \qquad (7)$$

where n_e represents the electron density, T_e the electron temperature, ξ the ratio of power coupled to electrons to the total power (electrons and ions) coupled to the plasma, e the elementary charge, P_{in} the input power, N_r the number of electron impact reactions, ε_i and R_i the electron energy loss due to the ith electron impact reaction (including electron-neutral momentum transfer collision) and the corresponding reaction rate, ε_e and ε_p the energy lost per electron and ion escaping the plasma across the sheaths.

Equation (1) and (7) are integrated using COMSOL chemical engineering module to solve for the time evolution of the electron temperature and densities of species.

3. Simulation results of the full model

In order to investigate the plasma chemistry of He+Air CAPs, the following cases of air admixture were considered in the study: 100, 200, 500, 1000, 2000, 5000 and 10000 ppm. This range accounts for the typical air concentrations encountered in most applications. The simulation results are discussed below.

A. Densities of reactive species as a function of air concentration

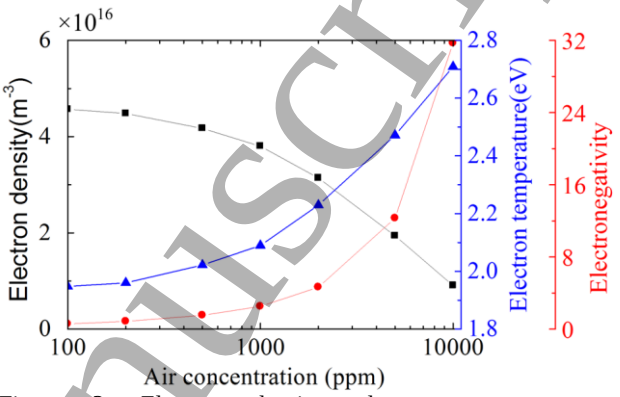

Figure 3. Electron density, electron temperature and electronegativity as a function of air concentration in the feed gas (—■—: Electron density; —▲—: Electron temperature; —●—: Electronegativity)

The dependence of the electron density, electron temperature and electronegativity on the air concentration is shown in Figure 3. As the air concentration increases from 100 ppm to 10000 ppm, the electron density decreases from 4.6×10^{16} to 9.1×10^{15} m^{-3}, while the electron temperature increases from 1.95 eV to 2.71 eV. It is noted that the electron temperature here is similar with that in previous reports of $He+H_2$ (~2.5eV), $He+O_2$ (~2.4 eV) and $He+O_2$+air (~2.4 eV) plasmas[33,10,34].

The densities of cations generated in He+Air CAPs are shown in Figure 4. For clarity, these are presented in two graphs: one showing the density of oxygen-free cations (Figure 4(a)) and another one showing the oxygen-containing cations (Figure 4(b)). In both graphs, the total concentration of cations is illustrated by a dotted line and it can be seen that the cation density rises from 7.2×10^{16} to 3.0×10^{17} m^{-3} when the air concentration in the admixture increases from 100 to 10000 ppm. For oxygen-containing cations, the densities of O_4^+, H_3O^+, NO^+ and NO_2^+ increase with the air concentration, whereas the density of other species decreases. For oxygen-free cations, the density as a function of the air concentration in the admixture shows monotonous decrease trend except for He^+, which increases obviously as the air concentration increases. This trend is mainly driven by the increasing electron-impact ionization of He with the increasing electron temperature (Figure 3). At low air concentration ([air]<150 ppm), O_2^+ is the most abundant cation. As the air content increases, NO^+ becomes dominant and at high air concentration ([air]>2000 ppm) NO_2^+ becomes the dominant ion. O_4^+ is not the most abundant cation, but it has a relative large density for all air

concentrations considered in the study. In He+O_2 plasmas with humid air impurity, O_4^+ was reported to be the most abundant cation [34].

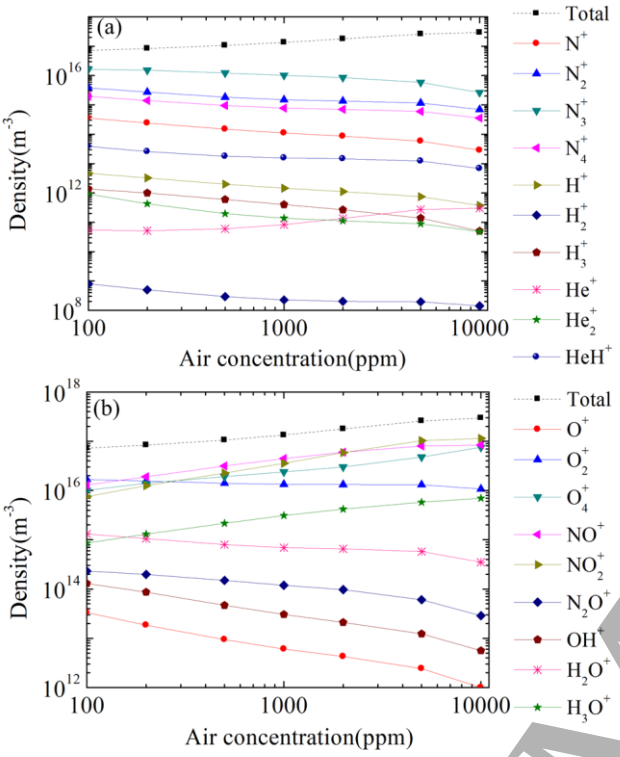

Figure 4. Densities of cations as a function of air concentration: (a) oxygen-free cations; (b) oxygen-containing cations

Similarly to the case of cations, the total anion density increases from 2.7×10^{16} to 2.9×10^{17} m^{-3} when the air concentration rises from 100 to 10000 ppm (Figure 5). It is noted that the electronegativity i.e. the ratio of anion density to electron density, increases with the concentration of air in the feed gas, and the plasma becomes electronegative for air concentrations above 1000 ppm (Figure 3).

The concentration of some anions, such as NO_3^-, NO_2^-, O_4^-, H^- and O_3^-, increase with the air concentration, whereas the density of NO^- first increases then decreases at high air concentration. Significantly, biologically relevant species such as O_2^- are found to be produced in relatively large quantities. The density of O_2^- decreases slightly as air content increases and it is the most abundant anion at low air concentrations (<300 ppm). As the air concentration increases above 300 ppm, NO_2^- and NO_3^- become the dominant species. It is noted that the density of NO_3^- has a significant increase of about three orders of magnitude as the air content increases from 100 to 10000 ppm. As a result, NO_3^- becomes the most abundant anion for [air]>2000 ppm. This is due to the large electron affinity (3.9 eV) of NO_3^- [65], and the increasing density of NO_2^- for charge transfer reactions to form NO_3^-.

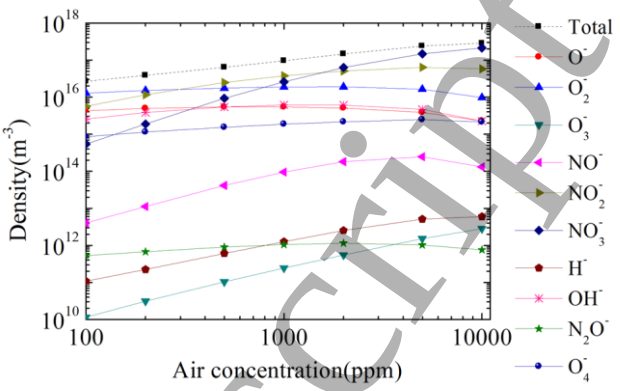

Figure 5. Densities of anions as a function of the air concentration in the feed gas

Figure 6 shows the densities of excited neutral species as a function of the air concentration. The dominant excited neutral species is O_2(a), of which the density increases from 9.8×10^{19} to 4.7×10^{21} m^{-3} as the air concentration in the feed gas changes from 100 to 10000 ppm. The density of O_2(a) is higher than that of the other excited species by several orders of magnitude, so its density curve nearly overlaps with that of the total excited neutral species (see Figure 6). This is due to the big electron collisional excitation cross section of O_2 to form O_2(a)[35]. O_2(a) is an important bio-active species on its own and it is also an important precursor for other bio-active species such as O_3. This suggests that O_2(a) is likely to play an important role in the biomedical applications of He+Air CAPs.

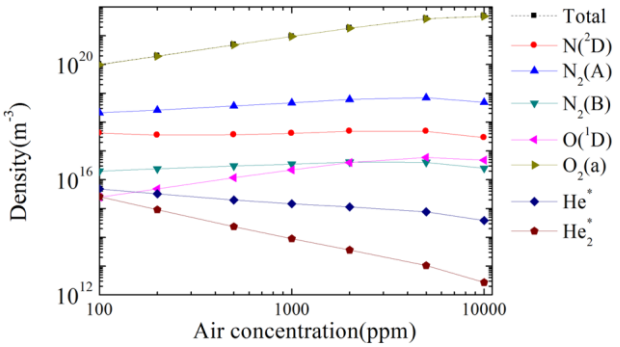

Figure 6. Density of excited neutral species as a function of the air concentration in the feed gas.

Albeit in much lower concentration, $O(^1D)$ has a very similar density trend to that of O_2(a). This is expected as both species are generated primarily by electron-neutral collisions with O_2. Dissociative excitation of O_2 to produce $O(^1D)$ requires 7.1 eV electrons, while only 0.98 eV is required for the excitation of O_2 to O_2(a). As a result, the density of $O(^1D)$ is lower than that of O_2(a) by more than four orders of magnitude.

As shown in Figure 6, He^* and He_2^* are present in low concentration but this does not mean that their production rates are small. Helium metastables have high potential energy, 19.8 eV for He^* and 18.4 eV for He_2^*, and therefore

they are capable of Penning ionizing air molecules (O_2: 12.06 eV; N_2: 15.58 eV; H_2O: 12.61 eV). These processes have large reaction rates and this is the main reason for the small concentration (<10^{16} m^{-3}) of helium metastables even when the air concentration is just 100 ppm. Their densities decrease monotonically with increasing air concentration by one and three orders of magnitude, respectively. Penning ionization has also been identified as an important ionization process in $He+H_2O$, $He+N_2$, $He+O_2$ plasmas [9,10,36].

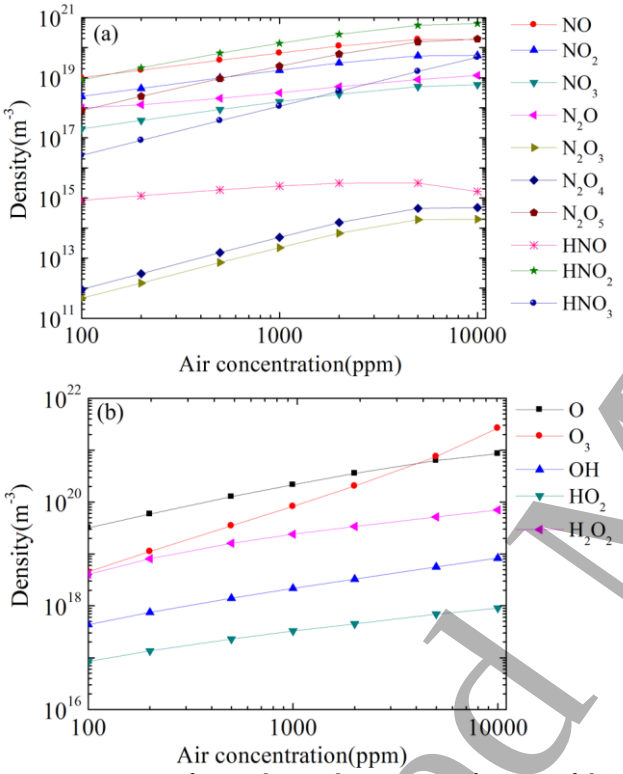

Figure 7. Density of ground neutral species as a function of the air concentration in the feed gas: (a) RNS (b) ROS

The density of ground-state neutral species generated in He+Air CAPs as a function of the air concentration are shown in Figure 7. These are divided into two groups: RNS (Figure 7a) and ROS (Figure 7b). The density of most ROS and RNS increases with the air content in the feedback gas. HNO is the only species that remains approximately constant for the air admixtures considered in this study. The most abundant ground-state species are O, O_3, NO and HNO_2. The density of O increases from 3.2×10^{19} to 8.5×10^{20} m^{-3} with the air concentration, and it is the most abundant ground-state ROS when [air]<5000 ppm. O has also been found to be the dominant ROS near the nozzle of argon plasma jets flowing into humid air[37]. O_3 becomes the dominant ROS when [air]>5000 ppm. For the RNS, NO is the most abundant one at low air concentrations ([air]<150 ppm), and then HNO_2 becomes the dominant RNS.

In addition, biological reactive species including OH, HO_2 and H_2O_2 have similar density trend, and their densities are all above 10^{17} m^{-3} in the whole air concentration range, indicating that these species would be important in applications of He+Air CAPs. The density of OH is lower than that of O by two orders of magnitude and this result agrees with observations made in air plasmas[26].

Although the helium concentration is typically at least 99% of the background gas in He+Air plasmas, helium-containing products (metastables and ions) have very low densities and in generally it can be said that most reactive species originate from air molecules. However, a comparison between an air plasma (ref [26]) and a He+Air plasma (this work) reveal substantial differences. For example, the most abundant ROS in air plasmas is O_3, but in He+Air plasmas O_3 only dominates when the air concentration is >5000 ppm. Instead, O is found to be more abundant than O_3 when the air concentration is <5000 ppm. This is primarily due to the lower density of O_2 in He+Air plasmas and since the main mechanism for ozone formation is the reaction of O with a reaction O_2, a lower molecular oxygen concentration favors the formation of O in He+Air plasmas. The composition of RNS also differs between the He+Air and the pure air plasmas. In particular, the densities of N_2O_5, N_2O and HNO_3 in air plasma are higher by several orders of magnitude than those in He+Air plasmas. Nonetheless, a larger amount of NO is produced in He+Air plasmas[26]. These trends observed in He+Air plasmas are similar to those found in Ar+Air plasmas [37] as in both cases the concentration of N_2 and O_2 are diluted by a noble gas. These results indicate that the presence of He can have a dramatic effect on the composition of the cocktail of ROS and RNS produced in air-containing plasmas.

As discussed above, helium ions and metastables have high production rates but their densities are low due to Penning processes and charge transfer reactions[9]. This leads to chemical pathways for the generation of reactive species that differ from those encountered in air plasmas. He+Air plasmas are also less electronegative than air discharges and this results in more electrons available for producing reactive species via excitation and dissociation of air molecules.

B. Power dissipation

Figure 8 shows the main channels in which power is dissipated in He+Air CAPs, as a function of the air concentration. The input power is mainly consumed in elastic collisions (momentum transfer collisions) between electrons and helium molecules. Despite the small energy transfer in each elastic collision, the large collisionality encountered in CAPs results in these collisions dominating the power balance. However, the percentage of energy dissipated via this channel decreases from 95% to 29% as the air concentration increases from 100 to 10000 ppm, because 1) the number of inelastic collisions increases with

the introduction of molecular gases (N_2, O_2 and H_2O), and 2) less power is coupled to electrons as the electronegativity of the plasma increases. The power consumed in electron-impact excitation processes becomes significant as the air content of the feed gas increases above 500 ppm and reaches 15% at [air]=10000 ppm. The following excitation reactions consume most of the power (the reaction number is from Appendix III):

$$e + N_2 \rightarrow N\left(^2D\right) + N + e \quad \text{(R5)}$$

$$e + N_2 \rightarrow N_2(A) + e \quad \text{(R3)}$$

$$e + N_2 \rightarrow N_2(B) + e \quad \text{(R4)}$$

$$e + O_2 \rightarrow O\left(^1D\right) + O + e \quad \text{(R8)}$$

The increasing power dissipation in electron-impact excitation contributes to the increasing densities of excited neutral species (see Figure 6). In comparison, the power dissipated in other inelastic processes, such as electron-impact ionization, is negligible. Due to the strong electronegative nature of O_2, increasing amount of power is coupled to ions as the air concentration in the feed gas increases. About 54% of the input power is consumed by ion Joule heating when [air]=10000 ppm. Power coupled to the ions has little effect on the plasma chemistry and contributes primarily to gas heating. As the power coupled to the electrons decreases with increasing air concentration, the electron density decreases as shown in Figure 3. These trends of power dissipations in He+Air CAPs are similar to those in He+O_2 and He+H_2 plasmas [10,33].

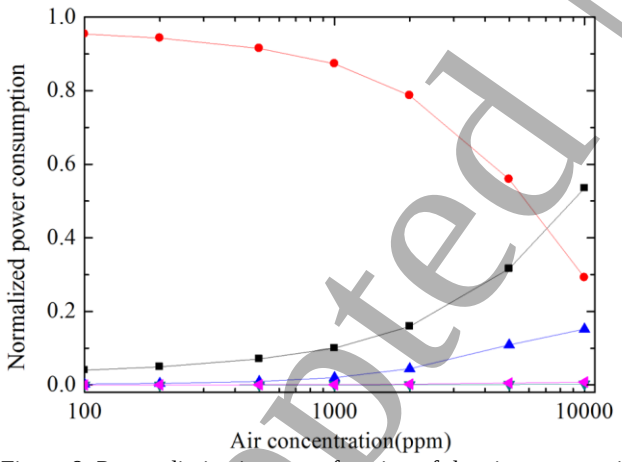

Figure 8. Power dissipations as a function of the air concentration (—■—: Ion Joule heating —●—: Elastic collisions —▲—: Electron excitation —▼—: Ionization —◀—: Other inelastic collisions)

4. Simulation results of the simplified model

The model used to obtained the results presented in section 3 incorporates 59 species and 866 reactions. While these can be easily handled by a global model, it is of interest to get a simplified model which can capture the main plasma chemistry but with a reduced set of species and reactions. This simplified chemistry model could then be used in more computationally demanding models to study other spatio-temporal dynamics not accounted for in zero dimensional models.

The criteria for selecting the main species and reactions from the full chemistry model are the same as those used in the study of He+H_2O and He+O_2 plasmas[9,10]. Briefly, once the simulation has reached steady state, only the species whose densities are larger than a threshold value are deemed important. Here the threshold is set to be the total density of the cations. Besides these main species, some intermediate species whose density doesn't reach the threshold but contribute significantly to the generation/loss of important species are also included in the simplified model.

Once the main species have been selected, the main reactions are chosen next by selecting the reactions whose total contribution to the particle balance of any of the main species exceeds a threshold value of 10% of the total generation (or loss) for that particular species. After this simplification process, a reduced set of species and chemical reactions consisting of 47 species and 109 volume reactions is obtained. The species in the simplified model are listed in table 3 and the main volume reactions are listed in Appendix III. The number of reactions in the simplified model is ~12% of those in the full model(original model).

A simplified global model is then developed with the reduced chemistry set and its accuracy and robustness are checked by comparing simulation results against the results obtained with the full global model.

Table 3. Main species

Type	Species
Cations	N^+, N_2^+, N_3^+, N_4^+, O^+, O_2^+, O_4^+, NO^+, NO_2^+, OH^+, H_2O^+, H_3O^+
anions	e, O^-, O_2^-, O_3^-, NO^-, NO_2^-, NO_3^-, OH^-,H^-
Metastables	He^*, He_2^*, $N(^2D)$, $N_2(A)$, $N_2(B)$, $O(^1D)$, $O_2(a)$
Grounded neutrals	He, H, N, O, O_3, NO, N_2O, NO_2, NO_3, N_2O_5, H_2, OH, HO_2, H_2O_2, HNO_2, HNO_3, N_2, O_2, H_2O

A. Accuracy and robustness

The accuracy and robustness of the simplified model can be assessed by comparing the composition of the plasma obtained with the simplified model against the results of the full model (59 species and 866 reactions).

Figure 9 compares the simulation results for the most important ROS and RNS, such as O, O_3, H_2O_2, OH, O_2^-, NO, NO_3, HNO_2 and HNO_3 for air concentrations varying from 100 to 10000 ppm. It can be seen that the results of the simplified model captures the trends predicted by the full model with a good agreement.

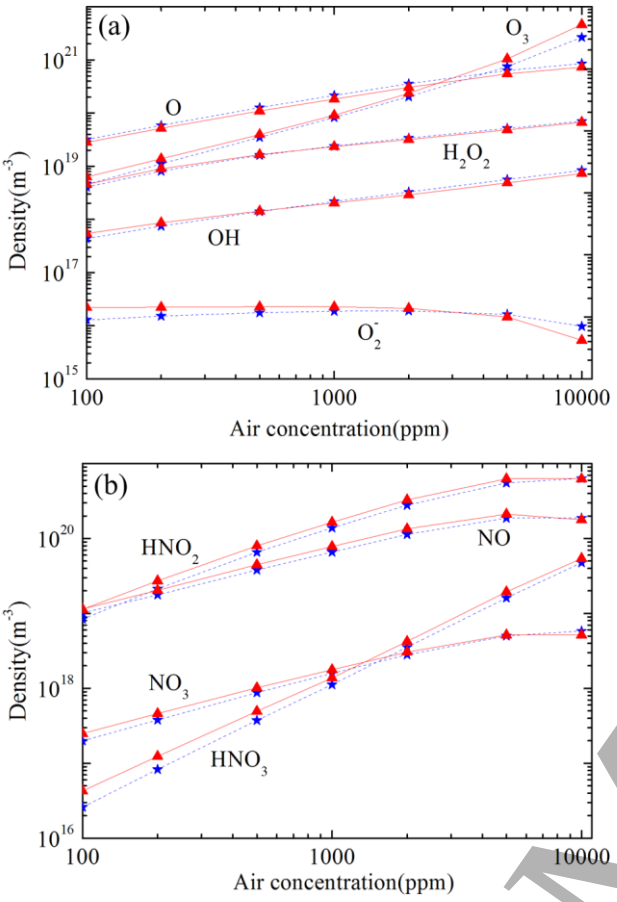

Figure 9. Density of selected (a) ROS and (b) RNS as a function of air concentration: ★: full model; ▲: simplified model

The validity and robustness of the simplified model is further investigated by comparing simulation results when the input power and gap distance are doubled. The relative error (RE) of the simplified model is quantified by calculating the root mean squared error for the density of all of the key species in the simplified model:

$$RE(\%) = \sqrt{\frac{1}{N_m}\sum_{i=1}^{N_m}\left(\frac{n_{is}-n_{id}}{\max\{n_{is},n_{id}\}}\right)^2} \times 100\% \qquad (5)$$

where N_m is the total number of species in the simplified model, n_{is} denotes the density of the ith main species obtained with the simplified model and n_{id} is the one obtained with the full model. The relative error incurred by the simplified model under different input power and discharge gap conditions as a function of the air content in the feed gas is shown in Figure 10. For all cases the error is less than 200% and lower errors (<60%) are observed for air concentrations >1000 ppm. These results suggest that the simplified model captures the main chemical pathways despite the changes in applied power and reactor geometry.

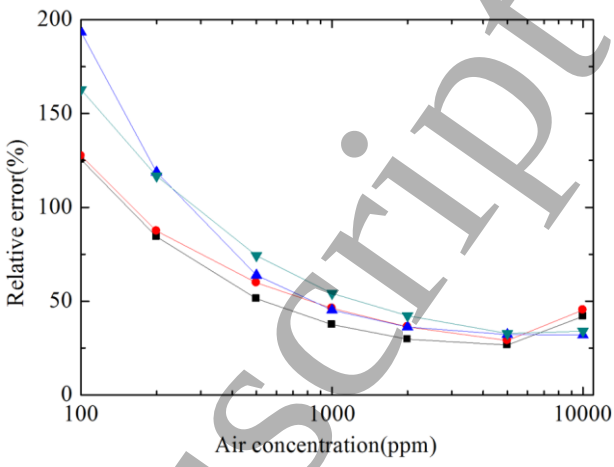

Figure 10. Accuracy of the simplified models with four different discharge conditions. ■: p=10 W/cm^3, g=2 mm; ●: p=10 W/cm^3, g=1 mm; ▲: p=20 W/cm^3, g=2 mm; ▼: p=20 W/cm^3, g=1 mm

B. Main chemical pathways of selected reactive species

Figure 11 illustrates the main pathways for the generation and loss of selected biologically relevant species in He+Air CAPs. RNS are shown on the left of the Figure and ROS in the middle and on the right. Simulation results presented in this section are obtained with the simplified model and we focus on the generation and loss of NO, HNO_2, HNO_3, HO_2, O, OH, H_2O_2, O_2^-, O_3 due to the high significance of these ROS and RNS.[5,38] The chemical pathways governing the interaction between these species are discussed next. The reaction numbers used in this section correspond to the reactions listed in Appendix III. It should be noted that in Figure 11 only the chemical pathways relevant to a selection of bio-active species (marked in red) are shown. Chemical pathways for the generation/loss of species not highlighted in red may be missing from Figure 11. For example, reaction R86: $N_2(A)+O \rightarrow O(^1D)+N_2$ is important for the production of O(^{1}D) but not shown in Figure 11.

Atomic oxygen (O) is an important ROS which is readily produced in plasmas but is not easily obtained by other means. At low air concentration, O is primarily produced by collisional relaxation reactions of O(^{1}D) (R54), followed by dissociation of O_2 by excited N_2 molecules (R83 and R87) and electron-impact dissociation of molecular oxygen (R8). Although the rate coefficient of R52 is about two orders of magnitude higher than the rate of R54, the N_2 concentration is much lower than the He concentration when the air concentration is low. As a result, despite its lower reaction rate constant, R54 is the dominant reaction for the production of O. At high air concentration, the dissociation of O_2 by excited N_2 molecules (R83 and R87) becomes the dominant chemical pathway for the production of O, followed by collisional relaxation reactions

(R52 and R54) and electron-impact dissociation (R8). This is different from CAPs operated in other gas environment (e.g. He+O_2, He+H_2O), where electron-impact dissociation of O_2 is the dominated mechanism for O production[10,39].

The present of excited N_2 in He+Air CAPs enhances the density of O(^{1}D) (R83) and consequently changes the main production pathway of the ground state O.

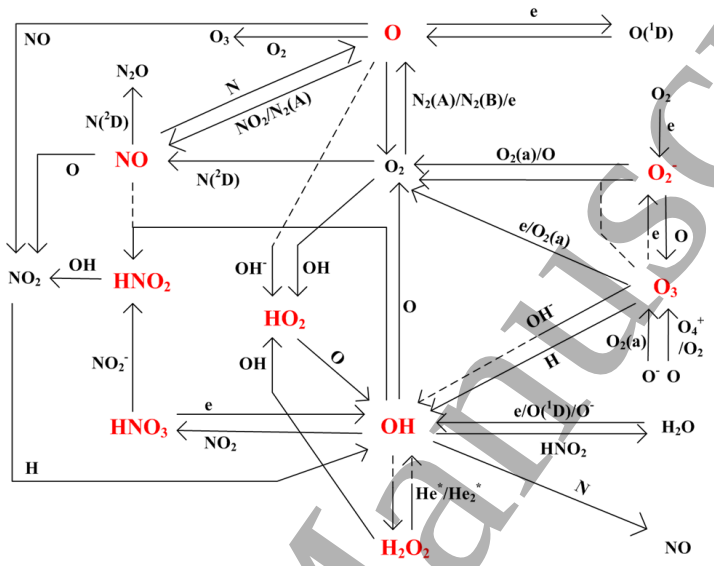

Figure 11. Main chemical pathways for the generation/loss of selected biologically relevant species (highlighted in red) in He+Air CAPs. Dotted lines represent secondary pathways whilst solid lines represent primary pathways. For example, the reaction between OH^- and O_3 is important pathway for the destruction of O_3 but unimportant for the production of OH.

$$e + O_2 \rightarrow O(^1D) + O + e \quad \text{(R8)}$$

$$O(^1D) + N_2 \rightarrow O + N_2 \quad \text{(R52)}$$

$$O(^1D) + He \rightarrow O + He \quad \text{(R54)}$$

$$N_2(A) + O_2 \rightarrow N_2 + 2O \quad \text{(R83)}$$

$$N_2(B) + O_2 \rightarrow N_2 + 2O \quad \text{(R87)}$$

Regarding the loss of O, the main pathway is electron excitation (R6) when the air concentration is low, followed by the reaction between O and NO_2 (R88), and some three-body reactions (R100, R101 and R102). At high air concentration, R88 and R102 become dominant for O destruction, followed by R100, R101 and R6. It is noted that the transformation of O to O_3 is mainly responsible for O destruction in the CAPs operated in other working gases such as He+O_2 and air[10,27]. However, the lower concentration of O_2 in the feed gas in He+Air CAPs limits the contribution of R101 (<12%) to the overall balance of O.

$$e + O \rightarrow O(^1D) + e \quad \text{(R6)}$$

$$O + NO_2 \rightarrow NO + O_2 \quad \text{(R88)}$$

$$He + 2O \rightarrow He + O_2 \quad \text{(R100)}$$

$$He + O_2 + O \rightarrow He + O_3 \quad \text{(R101)}$$

$$He + NO + O \rightarrow He + NO_2 \quad \text{(R102)}$$

Superoxide (O_2^-) is a well-known oxidizer in biological systems. In He+Air CAPs, O_2^- is mainly produced by electron impact attachment (R13) and dissociative attachment (R15). This is different from the main pathway observed in He+O_2 CAPs, in which the reaction $O+O_3^- \rightarrow O_2^- + O_2$ is important for the production of O_2^-[40]. In He+Air plasmas, however, due to the low density of O_3^- this mechanism is negligible.

$$e + O_2 \rightarrow O_2^- \quad \text{(R13)}$$

$$e + O_3 \rightarrow O_2^- + O \quad \text{(R15)}$$

O_2^- is mainly destroyed by collisional detachment (R56-R58), followed by charge transfer (R40, R41). R58 is the dominant reaction for the destruction of O_2^- at low air concentration, but R56 becomes the dominant mechanism at high air concentration as the density of O_3 increases rapidly.

$$O_2^- + O_3 \rightarrow O_3 + O_2 + \quad \text{(R56)}$$

$$O_2^- + O \rightarrow O_3 + e \quad \text{(R57)}$$

$$O_2^- + O_2(a) \rightarrow 2O_2 + e \quad \text{(R58)}$$

$$O_2^- + O \rightarrow O^- + O_2 \quad \text{(R40)}$$

$$O_2^- + O_3 \rightarrow O_3^- + O_2 \quad \text{(R41)}$$

A number of pathways contribute to the formation of hydroxyl radicals. At low air concentration OH is mainly produced by electron impact dissociation (R11 and R18), charge transfer (R37), and some reactions between neutral species (R91 and R97). However, when the air concentration is higher than 2000 ppm, R18, R93 and R95 become the dominant pathways for the production of OH radicals. This is different to He+H_2O CAPs, in which electron impact dissociation (R11) is always the most dominant reaction for OH production[23].

$$e + H_2O \rightarrow OH + H + e \quad \text{(R11)}$$

$$e + HNO_3 \rightarrow NO_2^- + OH \quad \text{(R18)}$$

$$O^- + H_2O \rightarrow OH^- + OH \quad \text{(R37)}$$

$$O + HO_2 \rightarrow OH + O_2 \quad \text{(R91)}$$

$$O(^1D) + H_2O \rightarrow 2OH \quad \text{(R93)}$$

$$O_3 + H \rightarrow OH + O_2 \quad \text{(R95)}$$

$$NO_2 + H \rightarrow OH + NO \quad \text{(R97)}$$

Regarding the loss of OH, R76 is the most responsible at low air concentration, followed by R90, R106 and R108. At high air concentration, R99 becomes important due to the increasing concentration of HNO_2, while R76 becomes unimportant because the density of N decreases with the increasing air concentration.

$$N + OH \rightarrow H + NO \quad \text{(R76)}$$

$$O + OH \rightarrow H + O_2 \quad \text{(R90)}$$

$$OH + HNO_2 \rightarrow NO_2 + H_2O \quad \text{(R99)}$$

$$He + NO + OH \rightarrow He + HNO_2 \quad \text{(R106)}$$

$$He + NO_2 + OH \rightarrow He + HNO_3 \quad \text{(R108)}$$

At low air concentration, HO_2 is mainly produced as a result of electron detachment of OH^- upon collision with O (R59). Other reactions with a significant contribution include R103 and R98. At high air concentration, R103 becomes the dominate process and accounts for 84% of the total HO_2 production, followed by R59 and R98.

$$OH^- + O \rightarrow HO_2 + e \quad \text{(R59)}$$

$$OH + H_2O_2 \rightarrow HO_2 + H_2O \quad \text{(R98)}$$

$$He + H + O_2 \rightarrow He + HO_2 \quad \text{(R103)}$$

Regarding the loss of HO_2, the primary channel is quenching with atomic oxygen (R91), which accounts for more than 90% of the HO_2 destruction for all the air concentrations considered in the study.

$$O + HO_2 \rightarrow OH + O_2 \quad \text{(R91)}$$

O_3 is an important ROS produced in many CAPs and typically it is produced by three-body reactions involving O and O_2[34,40] (R101). In He+Air plasma, however, this reaction is significant for the production of O_3 only at high air concentration. At air concentrations below 200 ppm, it is found that R55 and R29 account for most of the O_3 production. R57 is also significant in the whole range of air concentrations considered in this study.

$$O^- + O_2(a) \rightarrow O_3 + e \quad \text{(R55)}$$

$$O_2^- + O \rightarrow O_3 + e \quad \text{(R57)}$$

$$O_4^+ + O \rightarrow O_2^+ + O_3 \quad \text{(R29)}$$

$$He + O_2 + O \rightarrow He + O_3 \quad \text{(R101)}$$

Regarding the loss of ozone, O_3 is primarily consumed via electron impact dissociative detachment (R16) at low air concentration. Other contributing reactions are R12 and R46. At high air concentration, the dominant pathways for O_3 destruction are R94, R95 and R12.

$$e + O_3 \rightarrow O + O_2 + e \quad \text{(R12)}$$

$$e + O_3 \rightarrow O^- + O_2 \quad \text{(R16)}$$

$$OH^- + O_3 \rightarrow O_3^- + OH \quad \text{(R46)}$$

$$O_2(a) + O_3 \rightarrow O + 2O_2 \quad \text{(R94)}$$

$$O_3 + H \rightarrow OH + O_2 \quad \text{(R95)}$$

The production of hydrogen peroxide is driven by the three body reaction R104. This is the same mechanism observed in He+H_2O [9] and air plasmas[27].

$$He + 2OH \rightarrow He + H_2O_2 \quad \text{(R104)}$$

The loss of H_2O_2 at low air concentration is primarily driven by Penning ionization reactions (R66 and R71). This contrasts with the dissociative reactions observed in CAPs operated in Ar [25] and it is the result of the higher energy of helium metastables (He^* 19.8 eV and He_2^* 18.4 eV). As the air content in the feed gas is increased, the density of He^* and He_2^* decrease (see Figure 6) and at high air content R98 becomes the dominant process.

$$He^* + H_2O_2 \rightarrow He + OH + OH^+ + e \quad \text{(R66)}$$

$$He_2^* + H_2O_2 \rightarrow 2He + OH + OH^+ + e \quad \text{(R71)}$$

$$H_2O_2 + OH \rightarrow HO_2 + H_2O \quad \text{(R98)}$$

Formation of NO is primarily driven by heavy particle collisions. At low air concentration, the main channel for the production of NO is R88, R79 and R85. As the air content in the feed gas increases, the contribution of R88 becomes the dominant process when [air]>200 ppm. It is noted that R88 is also found important for NO production in He+O_2+humid air plasmas[34], and R85 in Ar+Air plasmas[37].

$$O_2 + N\left(^2D\right) \rightarrow NO + O\left(^1D\right) \quad \text{(R79)}$$

$$O + NO_2 \rightarrow NO + O_2 \quad \text{(R88)}$$

$$N_2(A) + O \rightarrow NO + N\left(^2D\right) \quad \text{(R85)}$$

Regarding the loss of NO, at low air concentration, quenching by atomic nitrogen (R74) is the most important channel. At high air concentration ([air]>200 ppm), quenching by atomic oxygen (R102) becomes the dominate pathway. NO destruction by excited nitrogen atoms (R77) has a small but not negligible contribution (1-10%) for all the air concentrations studied in this work. It is interesting to note that N_2(D) and O are responsible for the destruction of NO, but on the other hand they are the precursors of NO as discussed above.

$$N + NO \rightarrow N_2 + O \quad \text{(R74)}$$

$$N\left(^2D\right) + NO \rightarrow N_2O \quad \text{(R77)}$$

$$He + NO + O \rightarrow He + NO_2 \quad \text{(R102)}$$

As for HNO_2, R106 is the primary pathway for the production of HNO_2 and it accounts for over 80% of the HNO_2 production for all the air concentrations considered in the study. HNO_2 is primarily quenched by hydroxyl radicals (R99). The dominant pathways for the production and loss of HNO_2 (R106 and R99) are found to be the same as in air plasmas[27] and Ar+Air plasmas[37]. It is interesting to note that OH plays an crucial role in both the production and destruction of HNO_2.

$$He + NO + OH \rightarrow He + HNO_2 \quad \text{(R106)}$$

$$HNO_2 + OH \rightarrow NO_2 + H_2O \quad \text{(R99)}$$

Regarding HNO_3, the main chemical pathway for its production is the three body reaction R108:

$$He + NO_2 + OH \rightarrow He + HNO_3 \quad \text{(R108)}$$

Regarding the loss of HNO_3, most HNO_3 is consumed by electron impact dissociative attachment (R18). This reaction accounts for 95% of the HNO_3 destruction when the air content is 100 ppm and 68% when the air content is 10000 ppm. Interestingly, the reaction HNO_3 + OH →NO_3 + H_2O, a key process often believed to dominate the HNO_3 destruction[37,27], makes a relatively small contribution (<1%) in He+Air CAPs. This is because the rate coefficient of this reaction (1.3×10^{-19} m^3s^{-1}) is 4-5 orders of magnitude smaller than that of R18 (5×10^{-14} m^3s^{-1}). Besides dissociative attachment (R18), R45 also contributes to the destruction of HNO_3. This leads to the production of NO_3^-, which is the dominant anion at high air concentration (see Figure 5).

$$e + HNO_3 \rightarrow NO_2^- + OH \quad \text{(R18)}$$

$$NO_2^- + HNO_3 \rightarrow NO_3^- + HNO_2 \quad \text{(R45)}$$

4. Concluding remarks

A detailed global model of cold atmospheric-pressure He+Air CAPs that accounts for 59 species and 866 reactions has been developed. The model has been used to identify key species and chemical pathways as the air content in the feed gas varies from 100 to 10000 ppm. The model accounts for the radial diffusion in and out of the plasma region, taking into account the lifetime of each species and the different composition of the gas in and out of the plasma.

The density of reactive species and the power dissipation are calculated as a function of air concentration ranging from 100 to 10000 ppm. The total density of cations rises from 9.4×10^{16} to 3.6×10^{17} m^{-3} with the increasing air concentration from 100 to 10000 ppm, and the dominant cation changes from O_2^+ to NO^+ and then to NO_2^+. The total density of anions rises from 2.7×10^{16} to 2.9×10^{17} m^{-3}, and the dominant anion changes from O_2^- to NO_2^- and then to NO_3^-. The dominant ground state reactive oxygen species changes from O to O_3, and the dominant ground state reactive nitrogen species changes from NO to HNO_2. O_2(a) is the most abundant metastables, with a density that is several orders of magnitude larger than that of other metastables .

As the air content in the feed gas increases, the discharge becomes increasingly electronegative, and this has a significant effect on the way the power is dissipated in the discharge. At low air concentration, most energy is coupled to the electrons and dissipated primarily via momentum transfer collisions. Inelastic collisions consume an increasing amount of power as air is incorporated in the discharge, which leads to an increasing density of reactive species in the plasma. As the plasma becomes more electronegative, the energy lost via ion Joule heating increases and when the air content in the feed gas is 10000 ppm, it reaches ~54% of the total energy dissipated in the discharge.

Some significant differences between the plasma chemistry in He+Air plasmas and that of previously studied He+O_2, He+H_2O, Ar+Air and pure air plasmas have been revealed. Following a careful analysis of the different chemical pathways at play in He+Air discharges, the main species and reactions have been identified and a simplified discharge model capable of capturing the main physicochemical processes but with only a ~12% of the

complexity of the initial model has been created. The validity of the simplified model as the input power and /or the discharge gap size are doubled has also been verified.

From an application point of view, the densities and chemical pathways of biologically relevant species produced in He+Air CAPs provide a new insight into the plasma chemistry of these discharges to guide the operation and optimization of these plasmas in emerging biomedical, agricultural and environmental applications.

Acknowledgement

This work was supported by the National Science Foundation of China (Grant No. 51722705 and 51521065), and the Fundamental Research Funds for the Central Universities.

Appendix I: Helium-incorporated reactions in the full model

No.	Reaction	Rate coefficient[b]	Ref.
Electron impact momentum transfer			
1	$e + He \rightarrow e + He$	$f(T_e)$	9[a]
Electron impact ionization			
2	$e + He \rightarrow 2e + He^+$	$f(T_e)$	9[a]
3	$e + He^* \rightarrow 2e + He^+$	$f(T_e)$	9[a]
4	$e + He_2^* \rightarrow He_2^+ + 2e$	$9.75\times10^{-10} T_e^{0.71} \exp(-3.4/T_e)$	41
Electron impact excitation and de-excitation			
5	$e + He \rightarrow e + He^*$	$f(T_e)$	9[a]
6	$e + He^* \rightarrow He + e$	$7\times10^{-10} (11600T_e/300)^{0.5}$	42
7	$e + He_2^* \rightarrow e + 2He$	4×10^{-9}	43
Dissociative recombination			
8	$e + He^+ \rightarrow He$	2×10^{-12}	44
9	$e + He^+ \rightarrow He^*$	$6.76\times10^{-13} T_e^{-0.5}$	45
10	$e + He_2^+ \rightarrow 2He$	1×10^{-8}	41
11	$e + He_2^+ \rightarrow He_2^*$	1.5×10^{-16}	46
12	$e + He_2^+ \rightarrow He^* + He$	$8.9\times10^{-9} (11600T_e/T_g)^{-1.5}$	47
13	$e + HeH^+ \rightarrow H + He$	$1.1\times10^{-9} T_e^{-0.6}$	48
14	$2e + He^+ \rightarrow He + e$	$7\times10^{-20} (11600T_e/T_g)^{-4.5}$	49
15	$2e + He^+ \rightarrow He^* + e$	$6.0\times10^{-20} (11600T_e/T_g)^{-4}$	78
16	$2e + He_2^+ \rightarrow 2He + e$	$7\times10^{-20} (11600T_e/T_g)^{-4.5}$	49
17	$2e + He_2^+ \rightarrow He^* + He + e$	2.8×10^{-20}	50
18	$2e + He_2^+ \rightarrow He_2^* + e$	1.2×10^{-21}	50
19	$e + He + He^+ \rightarrow He^* + He$	1×10^{-27}	46
20	$e + He + He_2^+ \rightarrow 3He$	$2\times10^{-27} (11600T_e/T_g)^{-2.5}$	49
21	$e + He + He_2^+ \rightarrow He^* + 2He$	3.5×10^{-27}	50
22	$e + He + He_2^+ \rightarrow He_2^* + He$	1.5×10^{-27}	50
23	$e + O^+ + He \rightarrow O + He$	$6.45\times10^{-31} (11600T_e/T_g)^{-2.5}$	49
24	$e + N^+ + He \rightarrow N + He$	$2\times10^{-27} (11600T_e/T_g)^{-2.5}$	49
25	$e + N_2^+ + He \rightarrow N_2 + He$	$3.12\times10^{-23} / (11600T_e)^{1.5}$	34
26	$e + O_2^+ + He \rightarrow O_2 + He$	$3.12\times10^{-23} / (11600T_e)^{1.5}$	34
27	$e + NO^+ + He \rightarrow NO + M$	$3.12\times10^{-23} / (11600T_e)^{1.5}$	34
Electron impact attachment			
28	$e + O + He \rightarrow O^- + He$	10^{-31}	10

29	$e + O_2 + He \rightarrow O_2^- + He$	1×10^{-31}	10
30	$e + O_3 + He \rightarrow O_3^- + He$	1×10^{-31}	10
31	$e + OH + He \rightarrow OH^- + He$	3×10^{-31}	67
32	$e + NO + He \rightarrow NO^- + He$	8×10^{-31}	51
33	$e + NO_2 + He \rightarrow NO_2^- + He$	1.5×10^{-30}	52
34	$e + NO_3 + He \rightarrow NO_3^- + He$	1×10^{-30}	52
Ion-ion recombination			
35	$He^+ + O^- \rightarrow O + He$	$2\times10^{-7}\left(T_g/300\right)^{-1}$	45
36	$He^+ + O_2^- \rightarrow O_2 + He$	$2\times10^{-7}\left(T_g/300\right)^{-1}$	45
37	$He^+ + O_3^- \rightarrow O_3 + He$	$2\times10^{-7}\left(T_g/300\right)^{-1}$	45
38	$He^+ + H^- \rightarrow He + H$	$2.3\times10^{-7}\exp\left(T_g/300\right)^{-0.5}$	48
39	$He^+ + OH^- \rightarrow He + OH$	$2\times10^{-7}\left(T_g/300\right)^{-0.5}$	53
40	$He^+ + NO^- \rightarrow NO + He$	$2\times10^{-7}\left(T_g/300\right)^{-1}$	53
41	$He^+ + N_2O^- \rightarrow N_2O + He$	$2\times10^{-7}\left(T_g/300\right)^{-1}$	53
42	$He^+ + NO_2^- \rightarrow NO_2 + He$	$2\times10^{-7}\left(T_g/300\right)^{-1}$	53
43	$He^+ + NO_3^- \rightarrow NO_3 + He$	$2\times10^{-7}\left(T_g/300\right)^{-1}$	53
44	$He^+ + O_2^- \rightarrow O + O + He$	1×10^{-7}	45
45	$He^+ + O_3^- \rightarrow He + O + O_2$	1×10^{-7}	53
46	$He^+ + O_4^- \rightarrow He + 2O_2$	1×10^{-7}	53
47	$He^+ + OH^- \rightarrow He + O + H$	1×10^{-7}	53
48	$He^+ + NO^- \rightarrow N + O + He$	1×10^{-7}	53
49	$He^+ + N_2O^- \rightarrow N_2 + O + He$	1×10^{-7}	53
50	$He^+ + NO_2^- \rightarrow NO + O + He$	1×10^{-7}	53
51	$He^+ + NO_3^- \rightarrow NO + O_2 + He$	1×10^{-7}	53
52	$He_2^+ + O^- \rightarrow O + 2He$	1×10^{-7}	10,53
53	$He_2^+ + O_2^- \rightarrow O_2 + 2He$	1×10^{-7}	10,53
54	$He_2^+ + O_3^- \rightarrow O_3 + 2He$	1×10^{-7}	10,53
55	$He_2^+ + H^- \rightarrow H + 2He$	1×10^{-7}	53
56	$He_2^+ + OH^- \rightarrow OH + 2He$	1×10^{-7}	53
57	$He_2^+ + NO^- \rightarrow NO + 2He$	1×10^{-7}	53
58	$He_2^+ + N_2O^- \rightarrow N_2O + 2He$	1×10^{-7}	53
59	$He_2^+ + NO_2^- \rightarrow NO_2 + 2He$	1×10^{-7}	53

60	$He_2^+ + NO_3^- \rightarrow NO_3 + 2He$	1×10^{-7}	53
61	$HeH^+ + O^- \rightarrow OH + He$	1×10^{-7}	53
62	$HeH^+ + O_2^- \rightarrow HO_2 + He$	1×10^{-7}	53
63	$HeH^+ + O_3^- \rightarrow H + O_3 + He$	1×10^{-7}	53
64	$HeH^+ + H^- \rightarrow H_2 + He$	1×10^{-7}	53
65	$HeH^+ + OH^- \rightarrow H_2O + 2He$	1×10^{-7}	53
66	$HeH^+ + NO^- \rightarrow HNO + He$	1×10^{-7}	53
67	$HeH^+ + N_2O^- \rightarrow H + N_2O + He$	1×10^{-7}	53
68	$HeH^+ + NO_2^- \rightarrow HNO_2 + He$	1×10^{-7}	53
69	$HeH^+ + NO_3^- \rightarrow HNO_3 + He$	1×10^{-7}	53
70	$He_2^+ + O_2^- \rightarrow O + O + 2He$	1×10^{-7}	53
71	$He_2^+ + O_3^- \rightarrow O_2 + O + 2He$	1×10^{-7}	53
72	$He_2^+ + O_4^- \rightarrow 2O_2 + 2He$	1×10^{-7}	53
73	$He_2^+ + OH^- \rightarrow O + H + 2He$	1×10^{-7}	53
74	$He_2^+ + NO^- \rightarrow N + O + 2He$	1×10^{-7}	53
75	$He_2^+ + N_2O^- \rightarrow N_2 + O + 2He$	1×10^{-7}	53
76	$He_2^+ + NO_2^- \rightarrow NO + O + 2He$	1×10^{-7}	53
77	$He_2^+ + NO_3^- \rightarrow NO + O_2 + 2He$	1×10^{-7}	53
78	$HeH^+ + O_2^- \rightarrow H + O + O + He$	1×10^{-7}	53
79	$HeH^+ + O_3^- \rightarrow HO_2 + O + He$	1×10^{-7}	53
80	$HeH^+ + O_4^- \rightarrow HO_2 + O_2 + He$	1×10^{-7}	53
81	$HeH^+ + OH^- \rightarrow O + H_2 + He$	1×10^{-7}	53
82	$HeH^+ + NO^- \rightarrow H + N + O + He$	1×10^{-7}	53
83	$HeH^+ + N_2O^- \rightarrow H + N_2 + O + He$	1×10^{-7}	53
84	$HeH^+ + NO_2^- \rightarrow HNO + O + He$	1×10^{-7}	53
85	$HeH^+ + NO_3^- \rightarrow HNO + O_2 + He$	1×10^{-7}	53
Charge transfer			
86	$He^+ + O \rightarrow O^+ + He$	$5.0\times10^{-11}\left(T_g/300\right)^{0.5}$	45
87	$He^+ + O(^1D) \rightarrow O^+ + He$	$5\times10^{-11}\left(T_g/300\right)^{0.5}$	45
88	$He^+ + O_2(a) \rightarrow O_2^+ + He$	$3.3\times10^{-11}\left(T_g/300\right)^{0.5}$	45
89	$He^+ + O_2 \rightarrow O_2^+ + He$	$3.3\times10^{-11}\left(T_g/300\right)^{0.5}$	45
90	$He^+ + O_2 \rightarrow O^+ + O + He$	$1.07\times10^{-9}\left(T_g/300\right)^{0.5}$	45

91	$He^+ + O_2(a) \rightarrow O^+ + O + He$	$1.07\times10^{-9}\left(T_g/300\right)^{0.5}$	45
92	$He^+ + O_3 \rightarrow O^+ + O_2 + He$	$1.07\times10^{-9}\left(T_g/300\right)^{0.5}$	45
93	$He^+ + H \rightarrow He + H^+$	1.9×10^{-15}	48
94	$He^+ + H \rightarrow HeH^+$	$1.58\times10^{-15}\left(T_g/300\right)^{-0.3}$	54
95	$He^+ + H_2 \rightarrow He + H_2{}^+$	7.2×10^{-15}	48
96	$He^+ + H_2 \rightarrow He + H + H^+$	$3.7\times10^{-14}\exp\left(-35/T_g\right)$	48
97	$He^+ + OH \rightarrow O^+ + H + He$	1.1×10^{-9}	48
98	$He^+ + H_2O \rightarrow H_2O^+ + He$	6.05×10^{-11}	48
99	$He^+ + H_2O \rightarrow H^+ + OH + He$	2.04×10^{-10}	48
100	$He^+ + H_2O \rightarrow OH^+ + H + He$	2.86×10^{-10}	48
101	$He^+ + N_2 \rightarrow N_2{}^+ + He$	6.0×10^{-10}	49
102	$He^+ + N_2 \rightarrow N + N^+ + He$	6.0×10^{-10}	49
103	$He^+ + NO \rightarrow NO^+ + He$	1.6×10^{-9}	55
104	$He^+ + NO \rightarrow O + N^+ + He$	1.25×10^{-9}	55
105	$He^+ + 2He \rightarrow He_2^+ + He$	$1.4\times10^{-31}\left(T_g/300\right)^{-0.6}$	69
106	$He_2{}^+ + O \rightarrow O^+ + 2He$	$1\times10^{-9}\left(T_g/300\right)^{0.5}$	10
107	$He_2{}^+ + O\left(^1D\right) \rightarrow O^+ + 2He$	$1\times10^{-9}\left(T_g/300\right)^{0.5}$	10
108	$He_2{}^+ + O_2 \rightarrow O_2^+ + 2He$	$1\times10^{-9}\left(T_g/300\right)^{0.5}$	10
109	$He_2{}^+ + O_2 \rightarrow O^+ + 2He + O$	1.05×10^{-9}	56
110	$He_2{}^+ + O_2(a) \rightarrow O_2^+ + 2He$	$1\times10^{-9}\left(T_g/300\right)^{0.5}$	10
111	$He_2{}^+ + O_3 \rightarrow O_2 + 2He + O^+$	$1\times10^{-9}\left(T_g/300\right)^{0.5}$	10
112	$He_2{}^+ + N_2 \rightarrow 2He + N_2{}^+$	1.2×10^{-9}	49
113	$He_2{}^+ + N_2 \rightarrow He_2^* + N_2{}^+$	1.4×10^{-9}	57
114	$He_2{}^+ + NO \rightarrow 2He + NO^+$	1.3×10^{-9}	55
115	$He_2{}^+ + H \rightarrow H^+ + 2He$	3.5×10^{-10}	9
116	$He_2{}^+ + H_2 \rightarrow HeH^+ + H + He$	1.76×10^{-10}	72
117	$He_2{}^+ + H_2 \rightarrow H_2{}^+ + 2He$	3.5×10^{-10}	72
118	$He_2{}^+ + OH \rightarrow OH^+ + 2He$	1.2×10^{-9}	9
119	$He_2^+ + H_2O \rightarrow O^+ + H_2 + 2He$	2.1×10^{-10}	58
120	$He_2^+ + H_2O \rightarrow OH^+ + H + 2He$	2.1×10^{-10}	58
121	$He_2^+ + H_2O \rightarrow H^+ + OH + 2He$	2.1×10^{-10}	58

122	$He_2^+ + H_2O \rightarrow HeH^+ + OH + He$	1.3×10^{-10}	58
123	$He_2^+ + H_2O \rightarrow H_2^+ + O + 2He$	2.1×10^{-10}	58
124	$HeH^+ + H \rightarrow H_2^+ + He$	9.1×10^{-10}	48
125	$HeH^+ + H_2 \rightarrow H_3^+ + He$	1.5×10^{-9}	48
126	$HeH^+ + H_2O \rightarrow H_3O^+ + He$	4.3×10^{-10}	59
127	$He^* + {He_2}^+ \rightarrow He^+ + 2He$	1×10^{-10}	65
128	$He^* + {O_2}^+ \rightarrow O + He + O^+$	1.0×10^{-10}	65
129	$He^* + {O_4}^+ \rightarrow O_2 + He + {O_2}^+$	1.0×10^{-10}	65
130	$He^* + H_2O^+ \rightarrow 2H + He + O^+$	1.0×10^{-10}	65
131	$He^* + H_3O^+ \rightarrow H + He + H_2O^+$	1.0×10^{-10}	65
132	$He^* + {N_2}^+ \rightarrow N + He + N^+$	1.0×10^{-10}	65
133	$He^* + {N_3}^+ \rightarrow N + He + {N_2}^+$	1.0×10^{-10}	65
134	$He^* + {N_4}^+ \rightarrow N_2 + He + {N_2}^+$	1.0×10^{-10}	65
135	$He^* + NO^+ \rightarrow O + He + N^+$	5.0×10^{-11}	65
136	$He^* + NO^+ \rightarrow N + He + O^+$	5.0×10^{-11}	65
137	$He_2^* + {O_2}^+ \rightarrow O + 2He + O^+$	1×10^{-10}	65
138	$He_2^* + {O_4}^+ \rightarrow O_2 + 2He + {O_2}^+$	1×10^{-10}	65
139	$He_2^* + H_3O^+ \rightarrow H + 2He + H_2O^+$	1.0×10^{-10}	65
140	$He_2^* + H_3O^+ \rightarrow 3H + 2He + O^+$	1.0×10^{-10}	65
141	$He_2^* + {N_3}^+ \rightarrow N + 2He + {N_2}^+$	1.0×10^{-10}	65
142	$He_2^* + {N_4}^+ \rightarrow N_2 + 2He + {N_2}^+$	1.0×10^{-10}	65
143	$He^* + 2He \rightarrow He_2^* + He$	1.5×10^{-34}	78
144	$He + H^+ \rightarrow HeH^+$	$8.4\times10^{-19}\left(T_g/300\right)^{-4.5}$	60
145	$He + H_2^+ \rightarrow HeH^+ + H$	1.3×10^{-10}	48
146	$He + O^- + O_2 \rightarrow He + {O_3}^-$	$1.1\times10^{-30}(T_g/300)^{-1}$	49
147	$He + O^- + NO \rightarrow He + {NO_2}^-$	4.0×10^{-31}	56
148	$He + {O_2}^- + O_2 \rightarrow He + {O_4}^-$	$3.5\times10^{-31}(T_g/300)^{-1}$	49
149	$He + O^+ + O \rightarrow He + {O_2}^+$	$1\times10^{-29}\left(T_g/300\right)^{0.5}$	45
150	$He + O^+ + N \rightarrow He + NO^+$	1×10^{-29}	51
151	$He + O^+ + N_2 \rightarrow He + NO^+ + N$	$6\times10^{-29}\left(T_g/300\right)^{-2}$	49
152	$He + {O_2}^+ + O_2 \rightarrow He + {O_4}^+$	$3.9\times10^{-30}\left(T_g/300\right)^{-3.2}$	49
153	$He + N^+ + O \rightarrow He + NO^+$	1×10^{-29}	61

154	$He + N^+ + N \rightarrow He + N_2^+$	1×10^{-29}	53
155	$He + N^+ + N_2 \rightarrow He + N_3^+$	4.6×10^{-29}	62
156	$He + NO^+ + N \rightarrow He + N_2O^+$	$1\times10^{-29}(300/T_g)$	52
157	$He + N_2^+ + N_2 \rightarrow He + N_4^+$	$5\times10^{-29}\left(T_g/300\right)^{-1}$	49
158	$He + H^+ + H_2 \rightarrow He + H_3^+$	3.1×10^{-29}	51
Collisional relaxation			
159	$He + He^* \rightarrow 2He$	5.8×10^{-15}	63
160	$He + He_2^* \rightarrow 3He$	4.9×10^{-16}	47
161	$He + O(^1D) \rightarrow O + He$	1.0×10^{-13}	45
162	$He + O_2(a) \rightarrow O_2 + He$	$8\times10^{-21}\left(T_g/300\right)^{0.5}$	45
Collisional detachment			
163	$He + O^- \rightarrow He + O + e$	$2.5\times10^{-18}\left(T_g/300\right)^{0.6}$	64
164	$He + O_2^- \rightarrow He + O_2 + e$	$3.9\times10^{-10}\exp\left(-7400/T_g\right)$	10
165	$He + O_3^- \rightarrow He + O + O_2 + e$	3×10^{-10}	65
166	$He + H^- \rightarrow He + H + e$	$8\times10^{-12}\left(T_g/300\right)^{0.5}$	66
167	$He + OH^- \rightarrow He + OH + e$	$2\times10^{-9}\exp\left(-24030/T_g\right)$	67
168	$He + NO^- \rightarrow He + NO + e$	2.4×10^{-13}	68
169	$He^* + O^- \rightarrow O + He + e$	3.0×10^{-10}	65
170	$He^* + O_2^- \rightarrow O_2 + He + e$	3.0×10^{-10}	65
171	$He^* + O_3^- \rightarrow O_3 + He + e$	3.0×10^{-10}	65
172	$He^* + O_4^- \rightarrow 2O_2 + He + e$	3.0×10^{-10}	65
173	$He^* + H^- \rightarrow H + He + e$	2.0×10^{-10}	65,33
174	$He^* + OH^- \rightarrow OH + He + e$	3.0×10^{-10}	65
175	$He^* + NO^- \rightarrow NO + He + e$	3×10^{-10}	65
176	$He^* + NO_2^- \rightarrow NO_2 + He + e$	3×10^{-10}	65
177	$He^* + N_2O^- \rightarrow N_2O + He + e$	3×10^{-10}	65
178	$He^* + NO_3^- \rightarrow He + NO + O_2 + e$	3×10^{-10}	65
179	$He_2^* + O^- \rightarrow O + 2He + e$	3×10^{-10}	65
180	$He_2^* + O_2^- \rightarrow O_2 + 2He + e$	3×10^{-10}	65
181	$He_2^* + O_3^- \rightarrow O_3 + 2He + e$	3×10^{-10}	65
182	$He_2^* + O_4^- \rightarrow 2O_2 + 2He + e$	3×10^{-10}	65
183	$He_2^* + H^- \rightarrow H + 2He + e$	2.0×10^{-10}	65,33
184	$He_2^* + OH^- \rightarrow OH + 2He + e$	3×10^{-10}	65

185	$He_2^* + NO^- \rightarrow NO + 2He + e$	3×10^{-10}	65
186	$He_2^* + NO_2^- \rightarrow NO_2 + 2He + e$	3×10^{-10}	65
187	$He_2^* + N_2O^- \rightarrow N_2O + 2He + e$	3×10^{-10}	65
188	$He_2^* + NO_3^- \rightarrow 2He + NO + O_2 + e$	3×10^{-10}	65
Penning ionization			
189	$2He^* \rightarrow He_2^+ + e$	$2.03\times10^{-9}\left(T_g/300\right)^{0.5}$	69
190	$2He^* \rightarrow He^+ + He + e$	$8.7\times10^{-10}\left(T_g/300\right)^{0.5}$	69
191	$He^* + He_2^* \rightarrow He^+ + 2He + e$	5×10^{-10}	78
192	$He^* + He_2^* \rightarrow He_2^+ + He + e$	2×10^{-9}	78
193	$2He_2^* \rightarrow He^+ + 3He + e$	3×10^{-10}	78
194	$2He_2^* \rightarrow He_2^+ + 2He + e$	1.2×10^{-9}	50
195	$He^* + O(^1D) \rightarrow O^+ + He + e$	$3.96\times10^{-10}\left(T_g/300\right)^{0.17}$	70
196	$He^* + O \rightarrow O^+ + He + e$	$3.96\times10^{-10}\left(T_g/300\right)^{0.17}$	70
197	$He^* + O_2 \rightarrow O_2^+ + He + e$	$2.54\times10^{-10}\left(T_g/300\right)^{0.5}$	45
198	$He^* + O_3 \rightarrow O_2^+ + O + He + e$	2.6×10^{-10}	78
199	$He^* + H \rightarrow H^+ + He + e$	1.1×10^{-9}	71
200	$He^* + H_2 \rightarrow H_2^+ + He + e$	2.9×10^{-11}	72,73
201	$He^* + H_2 \rightarrow H + HeH^+ + e$	3×10^{-12}	72,73
202	$He^* + OH \rightarrow OH^+ + He + e$	7.8×10^{-10}	9
203	$He^* + H_2O \rightarrow H_2O^+ + He + e$	6.6×10^{-10}	59
204	$He^* + H_2O \rightarrow He + OH^+ + H + e$	1.5×10^{-10}	74,59
205	$He^* + H_2O \rightarrow He + OH + H^+ + e$	2.6×10^{-11}	74,59
206	$He^* + H_2O \rightarrow HeH^+ + OH + e$	8.5×10^{-12}	74,59
207	$He^* + H_2O_2 \rightarrow He + OH^+ + OH + e$	7.8×10^{-10}	9
208	$He^* + N_2 \rightarrow N^+ + N + He + e$	1×10^{-10}	65
209	$He^* + N_2 \rightarrow N_2^+ + He + e$	5×10^{-11}	47
210	$He_2^* + O \rightarrow 2He + O^+ + e$	3.6×10^{-10}	78
211	$He_2^* + O(^1D) \rightarrow 2He + O^+ + e$	3.6×10^{-10}	78
212	$He_2^* + O_2 \rightarrow 2He + O_2^+ + e$	3.6×10^{-10}	78
213	$He_2^* + O_3 \rightarrow 2He + O_2^+ + O + e$	3.6×10^{-10}	78
214	$He_2^* + H \rightarrow 2He + H^+ + e$	2.2×10^{-10}	9
215	$He_2^* + H_2 \rightarrow H_2^+ + 2He + e$	2.2×10^{-10}	75

216	$He_2^* + OH \rightarrow OH^+ + 2He + e$	6×10^{-10}	9
217	$He_2^* + H_2O \rightarrow H_2O^+ + 2He + e$	6×10^{-10}	76
218	$He_2^* + H_2O_2 \rightarrow OH^+ + OH + 2He + e$	6×10^{-10}	9
219	$He_2^* + N_2 \rightarrow 2He + N_2^+ + e$	3×10^{-11}	77
Neutral reactions			
220	$He + O_3 \rightarrow He + O + O_2$	$1.56\times10^{-9}\exp\left(-11400/T_g\right)$	78,45
221	$He + 2O \rightarrow He + O_2$	$1.3\times10^{-32}\left(T_g/300\right)^{-1}\exp\left(-170/T_g\right)$	45
222	$He + O_2 + O \rightarrow He + O_3$	$3.4\times10^{-34}\left(T_g/300\right)^{-1.2}$	45
223	$He + N + O \rightarrow He + NO$	$1.76\times10^{-31}T_g^{-0.5}$	72
224	$He + NO + O \rightarrow He + NO_2$	1×10^{-31}	79
225	$He + N + N \rightarrow He + N_2$	$7.6\times10^{-34}\exp\left(500/T_g\right)$	65
226	$He + H + O \rightarrow He + OH$	$3.2\times10^{-33}\left(T_g/300\right)^{-1}$	10
227	$He + H + OH \rightarrow He + H_2O$	$1.56\times10^{-31}\left(T_g/300\right)^{-2.6}$	9,80
228	$He + 2H \rightarrow He + H_2$	$5.8\times10^{-33}\left(T_g/300\right)^{-1}$	81
229	$He + H + O_2 \rightarrow He + HO_2$	$2\times10^{-32}\left(T_g/300\right)^{-0.8}$	81
230	$He + 2OH \rightarrow He + H_2O_2$	$3.96\times10^{-31}(T_g/300)^{-3.2}$	81
231	$He + 2O \rightarrow O_2(a) + He$	9.88×10^{-35}	45
232	$He + O + NO_2 \rightarrow He + NO_3$	$9\times10^{-32}(300/T_g)^2$	82
233	$He + O(^1D) + N_2 \rightarrow He + N_2O$	9×10^{-37}	83
234	$He + NO + NO_2 \rightarrow He + N_2O_3$	$3.09\times10^{-34}(300/T_g)^{7.7}$	84
235	$He + NO + OH \rightarrow He + HNO_2$	$7.4\times10^{-31}(300/T_g)^{2.4}$	82
236	$He + NO + H \rightarrow He + HNO$	$1\times10^{-32}\exp(300/T_g)$	85
237	$He + NO_2 + NO_2 \rightarrow He + N_2O_4$	$1.17\times10^{-33}(300/T_g)^{3.8}$	84
238	$He + NO_2 + NO_3 \rightarrow He + N_2O_5$	$2.8\times10^{-30}(300/T_g)^{3.5}$	83
239	$He + NO_2 + OH \rightarrow He + HNO_3$	$2.2\times10^{-30}(300/T_g)^{2.9}$	82
240	$He + N_2O_3 \rightarrow He + NO + NO_2$	$1.03\times10^{-10}\exp(-2628/T_g)$	84
241	$He + N_2O_4 \rightarrow He + NO_2 + NO_2$	$1.09\times10^{-7}\exp(-4952/T_g)$	84
242	$He + N_2O_5 \rightarrow He + NO_2 + NO_3$	$1\times10^{-3}(300/T_g)^{3.5}\exp(-11000/T_g)$	83

T_e in eV, T_g in Kelvin

[a] The rate coefficient is obtained from EEDF using cross section from indicated reference.

[b] Rate coefficient is in cm^3/s for two-body reactions and cm^6/s for three-body reactions

Appendix Ⅱ : Sidewise loss of neutral species

The mass conservation for neutral species *i* is given by the following equation [32]:

$$\frac{dn_i(r,\varphi,z,t)}{dt} - D_i\nabla^2 n_i(r,\varphi,z,t) = S_i(r,\varphi,z,t) \quad \text{(A1)}$$

We are interested in the steady state solution and for simplicity we consider a 1-dimension problem in *r*. In this case, A1 reduces to:

$$-\frac{D}{r}\frac{d}{dr}\left(r\frac{dn}{dr}\right) = G - Kn \quad \text{(A2)}$$

where *G* is the average generation rate due to gas phase reactions (assumed to be constant) and *K* the reaction frequency for the destruction of species *i* (assuming a linear approximation).

To solve A2, we assume as boundary condition that the flux at *r=R* is the thermal flux:

$$-D\frac{dn}{dr}\Big|_{r=R} = 0.25n(R)v_{th} \quad \text{(A3)}$$

The solution to A2 will be the sum of solution to the homogeneous equation and a particular solution. A particular solution to A2 is:

$$n_p = \frac{G}{K} \quad \text{(A4)}$$

And the homogeneous equation can be re-written as follows:

$$\frac{d^2n}{dr^2} + \frac{1}{r}\frac{dn}{dr} - \frac{K}{D}n = 0 \Rightarrow$$
$$\frac{d^2n}{d\left(\sqrt{\frac{K}{D}}r\right)^2} + \frac{1}{\sqrt{\frac{K}{D}}r}\frac{dn}{d\left(\sqrt{\frac{K}{D}}r\right)} - n = 0 \quad \text{(A5)}$$

The solution of this homogeneous equation is:

$$n_h = AI_0\left(\sqrt{\frac{K}{D}}r\right) + BK_0\left(\sqrt{\frac{K}{D}}r\right) \quad \text{(A6)}$$

where I_0 is the modified zero-order Bessel function of the first kind and K_0 the modified zero-order Bessel function of the second kind. A and B are integration constants.

Since $K_0\left(\sqrt{K/D}r\right)$ diverges at r=0, B must be 0 for a physical solution.

Therefore the solution to Eq. A2 is

$$n(r) = n_p + n_h = \frac{G}{K} + AI_0\left(\sqrt{\frac{K}{D}}r\right) \quad \text{(A7)}$$

To determine the integration constant A, we impose the boundary condition A3:

$$-D\frac{dn}{dr}\Big|_{r=R} = -DAI_0'\left(\sqrt{\frac{K}{D}}r\right)\Big|_{r=R}$$
$$= -DA\sum_{m=1}\frac{2m\left(\sqrt{\frac{K}{D}}\right)^{2m}R^{2m-1}}{2^{2m}(m!)^2}$$
$$= -\sqrt{DK}A\sum_{m=1}\frac{2m\left(\sqrt{\frac{K}{D}}R\right)^{2m-1}}{2^{2m}(m!)^2} = 0.25\left(\frac{G}{K} + AI_0\left(\sqrt{\frac{K}{D}}R\right)\right)v_{th} \quad \text{(A8)}$$

And therefore the integration constant A is equal to:

$$A = -\frac{0.25\frac{G}{K}v_{th}}{\sqrt{DK}\sum_{m=1}\frac{2m\left(\sqrt{\frac{K}{D}}R\right)^{2m-1}}{2^{2m}(m!)^2} + 0.25I_0\left(\sqrt{\frac{K}{D}}R\right)v_{th}} \quad \text{(A9)}$$

Substituting A9 into A7, we obtain the solution to Eq. A2, i.e. the radial variation of the density for species *i*:

$$n(r) = \frac{G}{K}\left(1 - \frac{0.25v_{th}I_0\left(\sqrt{\frac{K}{D}}r\right)}{\sqrt{DK}\sum_{m=1}\frac{2m\left(\sqrt{\frac{K}{D}}R\right)^{2m-1}}{2^{2m}(m!)^2} + 0.25I_0\left(\sqrt{\frac{K}{D}}R\right)v_{th}}\right) \quad \text{(A10)}$$

The average density of species i across the radial direction (n_{ave}) is calculated by integrating Eq.A10 and then dividing the result by the electrode disk area. And then the ratio of the boundary density to the average density for species *i* is given by:

$$\frac{n(R)}{n_{ave}} = \frac{R^2\sqrt{DK}\sum_{m=1}\frac{2m\left(\sqrt{\frac{K}{D}}R\right)^{2m-1}}{2^{2m}(m!)^2}}{\int_0^R 2r\left(\sqrt{DK}\sum_{m=1}\frac{2m\left(\sqrt{\frac{K}{D}}R\right)^{2m-1}}{2^{2m}(m!)^2}+0.25I_0\left(\sqrt{\frac{K}{D}}R\right)v_{th}-0.25v_{th}I_0\left(\sqrt{\frac{K}{D}}r\right)\right)dr} \quad \text{(A11)}$$

The radial diffusion loss rate for species *i* is:

$$S_{d,i} = \frac{s}{V}\frac{1}{4}n_{ave}\frac{R^2\sqrt{DK}\sum_{m=1}\frac{2m\left(\sqrt{\frac{K}{D}}R\right)^{2m-1}}{2^{2m}(m!)^2}}{\int_0^R 2r\left(\sqrt{DK}\sum_{m=1}\frac{2m\left(\sqrt{\frac{K}{D}}R\right)^{2m-1}}{2^{2m}(m!)^2}+0.25I_0\left(\sqrt{\frac{K}{D}}R\right)v_{th}-0.25v_{th}I_0\left(\sqrt{\frac{K}{D}}r\right)\right)dr}v_{th} \quad \text{(A12)}$$

Appendix Ⅲ: main reactions for He+Air plasmas

No.	Reaction	Rate coefficient[b]	Ref.
Electron impact momentum transfer			
1	$e+He \rightarrow e+He$	$f(T_e)$	9[a]
Electron impact excitation and de-excitation			
2	$e+N \rightarrow N(^2D)+e$	$f(T_e)$	86[a]
3	$e+N_2 \rightarrow N_2(A)+e$	$f(T_e)$	87[a]
4	$e+N_2 \rightarrow N_2(B)+e$	$f(T_e)$	87[a]
5	$e+N_2 \rightarrow N(^2D)+N+e$	$f(T_e)$	34[a]
6	$e+O \rightarrow O(^1D)+e$	$f(T_e)$	88[a]
7	$e+O_2 \rightarrow O_2(a)+e$	$f(T_e)$	35[a]
8	$e+O_2 \rightarrow O(^1D)+O+e$	$f(T_e)$	89[a]
9	$e+H_2O \rightarrow H_2+O(^1D)+e$	$f(T_e)$	90[a]
10	$e+He \rightarrow e+He^*$	$f(T_e)$	9[a]
Electron impact dissociation			
11	$e+H_2O \rightarrow OH+H+e$	$f(T_e)$	91[a]
12	$e+O_3 \rightarrow O+O_2+e$	$f(T_e)$	92[a]
Electron impact attachment			
13	$e+O_2 \rightarrow O_2^-$	$f(T_e)$	93[a]
14	$e+O_2 \rightarrow O^-+O$	$f(T_e)$	94[a]
15	$e+O_3 \rightarrow O_2^-+O$	$f(T_e)$	95[a]
16	$e+O_3 \rightarrow O_2+O^-$	$f(T_e)$	95[a]
17	$e+H_2O \rightarrow H^-+OH$	$f(T_e)$	96[a]
18	$e+HNO_3 \rightarrow NO_2^-+OH$	5×10^{-8}	97
19	$e+NO+He \rightarrow NO^-+He$	8×10^{-31}	51
Ion-ion recombination			
20	$NO^+ + NO_3^- \rightarrow NO_3+NO$	$2\times10^{-7}\times\left(300/T_g\right)^{0.5}$	53
21	$NO_2^+ + NO_3^- \rightarrow NO_3+NO_2$	$2\times10^{-7}\times\left(300/T_g\right)^{0.5}$	97
Charge transfer			
22	$N_2^+ + H_2O \rightarrow H_2O^+ + N_2$	2.3×10^{-9}	51
23	$N_3^+ + O_2 \rightarrow O_2^+ + N+N_2$	2.3×10^{-11}	51
24	$N_3^+ + O_2 \rightarrow NO^+ + O+N_2$	2×10^{-11}	51
25	$N_3^+ + O_2 \rightarrow NO_2^+ + N_2$	4.4×10^{-11}	51
26	$N_4^+ + N_2 \rightarrow N_2^+ + 2N_2$	$2.1\times10^{-10}\times\exp(T_g/121)$	51
27	$N_4^+ + H_2O \rightarrow H_2O^+ + 2N_2$	3×10^{-9}	51
28	$O_2^+ + N_2O_5 \rightarrow NO_2^+ + NO_3+O_2$	8.8×10^{-10}	53
29	$O_4^+ + O \rightarrow O_2^+ + O_3$	3×10^{-10}	53

30	$O_4^+ + NO \rightarrow NO^+ + 2O_2$	6.8×10^{-10}	98
31	$NO^+ + N_2O_5 \rightarrow NO_2^+ + 2NO_2$	5.9×10^{-10}	53
32	$NO_2^+ + NO \rightarrow NO^+ + NO_2$	2.75×10^{-10}	99
33	$OH^+ + O_2 \rightarrow O_2^+ + OH$	5.9×10^{-10}	98
34	$H_2O^+ + O_2 \rightarrow O_2^+ + H_2O$	4.3×10^{-10}	51
35	$H_2O^+ + H_2O \rightarrow H_3O^+ + OH$	1.7×10^{-9}	51
36	$H_3O^+ + N_2O_5 \rightarrow NO_2^+ + HNO_3 + H_2O$	5.5×10^{-10}	52
37	$O^- + H_2O \rightarrow OH^- + OH$	1.4×10^{-9}	51
38	$O^- + O_2(a) \rightarrow O_2^- + O$	1×10^{-10}	51
39	$O^- + O_3 \rightarrow O_3^- + O$	8×10^{-10}	51
40	$O_2^- + O \rightarrow O^- + O_2$	3.3×10^{-10}	51
41	$O_2^- + O_3 \rightarrow O_3^- + O_2$	3.5×10^{-10}	51
42	$NO^- + O_2 \rightarrow O_2^- + NO$	5×10^{-10}	51
43	$NO_2^- + N_2O_5 \rightarrow NO_3^- + NO_3 + NO$	7×10^{-10}	51
44	$NO_2^- + NO \rightarrow NO^- + NO_2$	2.75×10^{-10}	99
45	$NO_2^- + HNO_3 \rightarrow NO_3^- + HNO_2$	1.6×10^{-9}	27
46	$OH^- + O_3 \rightarrow O_3^- + OH$	9×10^{-10}	100
47	$He + O^- + O_2 \rightarrow He + O_3^-$	$1.1\times10^{-30}\times(T_g/300)^{-1}$	101
48	$He + O^+ + N_2 \rightarrow He + NO^+ + N$	$6\times10^{-29}\left(T_g/300\right)^{-2}$	101
49	$He + O_2^+ + O_2 \rightarrow He + O_4^+$	$3.9\times10^{-30}\left(T_g/300\right)^{-3.2}$	101
50	$He + N_2^+ + N_2 \rightarrow He + N_4^+$	$5\times10^{-29}\left(T_g/300\right)^{-1}$	101
51	$He + N^+ + N_2 \rightarrow He + N_3^+$	4.6×10^{-29}	62
Collisional relaxation			
52	$O(^1D) + N_2 \rightarrow O + N_2$	$1.8\times10^{-11}\times\exp(107/T_g)$	82
53	$N_2(B) + N_2 \rightarrow N_2(A) + N_2$	5×10^{-11}	53
54	$He + O(^1D) \rightarrow O + He$	1.0×10^{-13}	45
Collisional detachment			
55	$O^- + O_2(a) \rightarrow O_3 + e$	3×10^{-10}	51
56	$O_2^- + O_3 \rightarrow O_3 + O_2 + e$	6×10^{-10}	102
57	$O_2^- + O \rightarrow O_3 + e$	1.5×10^{-10}	51
58	$O_2^- + O_2(a) \rightarrow 2O_2 + e$	2×10^{-10}	51
59	$OH^- + O \rightarrow HO_2 + e$	2×10^{-10}	100
60	$He + O_3^- \rightarrow He + O + O_2 + e$	3×10^{-10}	65

61	$He + H^- \rightarrow He + H + e$	$8\times10^{-18}\left(T_g/300\right)^{0.5}$	66
62	$He + NO^- \rightarrow He + NO + e$	2.4×10^{-13}	68
Penning ionization			
63	$He^* + O \rightarrow O^+ + He + e$	$3.96\times10^{-10}\left(T_g/300\right)^{0.17}$	70
64	$He^* + O_2 \rightarrow {O_2}^+ + He + e$	$2.54\times10^{-10}\left(T_g/300\right)^{0.5}$	45
65	$He^* + H_2O \rightarrow He + OH^+ + H + e$	1.5×10^{-10}	74
66	$He^* + H_2O_2 \rightarrow He + OH^+ + OH + e$	7.8×10^{-10}	9
67	$He^* + N_2 \rightarrow {N_2}^+ + He + e$	5×10^{-11}	47
68	$He^* + N_2 \rightarrow N^+ + N + He + e$	1×10^{-10}	65
69	${He_2}^* + O \rightarrow 2He + O^+ + e$	3.6×10^{-10}	78
70	${He_2}^* + O_2 \rightarrow 2He + {O_2}^+ + e$	3.6×10^{-10}	78
71	${He_2}^* + H_2O_2 \rightarrow OH^+ + OH + 2He + e$	6×10^{-10}	9
72	${He_2}^* + N_2 \rightarrow 2He + {N_2}^+ + e$	3×10^{-11}	77
radiation			
73	$N_2(B) \rightarrow N_2(A)$	1.25×10^{5}	103
Neutral reactions			
74	$N + NO \rightarrow N_2 + O$	$2.1\times10^{-11}\times\exp(100/T_g)$	82
75	$N + NO_2 \rightarrow N_2O + O$	$5.8\times10^{-12}\times\exp(220/T_g)$	82
76	$N + OH \rightarrow H + NO$	7.5×10^{-11}	51
77	$N(^2D) + NO \rightarrow N_2O$	6×10^{-11}	53
78	$N(^2D) + O_2 \rightarrow NO + O$	$1.5\times10^{-12}\times\left(T_g/300\right)^{0.5}$	53
79	$N(^2D) + O_2 \rightarrow NO + O(^1D)$	$6\times10^{-12}\times\left(T_g/300\right)^{0.5}$	53
80	$N_2(A) + N_2(A) \rightarrow N_2(B) + N_2$	4×10^{-10}	82
81	$N_2(A) + N_2O \rightarrow O + 2N_2$	8×10^{-11}	97
82	$N_2(A) + N_2O \rightarrow NO + N + N_2$	8×10^{-11}	97
83	$N_2(A) + O_2 \rightarrow N_2 + 2O$	$5\times10^{-12}\times\exp(-210/T_g)$	82
84	$N_2(A) + O_2 \rightarrow O_2(a) + N_2$	1×10^{-12}	97
85	$N_2(A) + O \rightarrow NO + N(^2D)$	7×10^{-12}	51
86	$N_2(A) + O \rightarrow O(^1D) + N_2$	2.3×10^{-11}	52
87	$N_2(B) + O_2 \rightarrow N_2 + 2O$	3×10^{-10}	51
88	$O + NO_2 \rightarrow NO + O_2$	$6.5\times10^{-12}\times\exp(120/T_g)$	82
89	$O + NO_3 \rightarrow O_2 + NO_2$	1.7×10^{-11}	82
90	$O + OH \rightarrow H + O_2$	$2.2\times10^{-11}\times\exp(-350/T_g)$	51
91	$O + HO_2 \rightarrow OH + O_2$	$8.3\times10^{-11}\times\exp(-500/T_g)$	51

92	$O(^1D) + H_2 \rightarrow OH + H$	1.1×10^{-10}	83
93	$O(^1D) + H_2O \rightarrow OH + OH$	2.2×10^{-10}	104
94	$O_2(a) + O_3 \rightarrow O + 2O_2$	$5.2\times10^{-11}\times\exp(-2840/T_g)$	82
95	$O_3 + H \rightarrow OH + O_2$	$2.8\times10^{-11}\times\left(T_g/300\right)^{0.75}$	51
96	$NO + NO_3 \rightarrow 2NO_2$	$1.8\times10^{-11}\times\exp(110/T_g)$	82
97	$NO_2 + H \rightarrow OH + NO$	1.47×10^{-10}	51
98	$OH + H_2O_2 \rightarrow HO_2 + H_2O$	$2.9\times10^{-12}\times\exp(-160/T_g)$	83
99	$OH + HNO_2 \rightarrow NO_2 + H_2O$	$1.8\times10^{-11}\times\exp(-390/T_g)$	27
100	$He + 2O \rightarrow He + O_2$	$1.3\times10^{-32}\left(T_g/300\right)^{-1}\exp\left(-170/T_g\right)$	45
101	$He + O_2 + O \rightarrow He + O_3$	$3.4\times10^{-34}\left(T_g/300\right)^{-1.2}$	45
102	$He + NO + O \rightarrow He + NO_2$	1×10^{-31}	79
103	$He + H + O_2 \rightarrow He + HO_2$	$2\times10^{-32}\left(T_g/300\right)^{-0.8}$	81
104	$He + 2OH \rightarrow He + H_2O_2$	$3.96\times10^{-31}(T_g/300)^{-3.2}$	81
105	$He + O + NO_2 \rightarrow He + NO_3$	$9\times10^{-32}(300/T_g)^2$	82
106	$He + NO + OH \rightarrow He + HNO_2$	$7.4\times10^{-31}(300/T_g)^{2.4}$	82
107	$He + NO_2 + NO_3 \rightarrow He + N_2O_5$	$2.8\times10^{-30}(300/T_g)^{3.5}$	83
108	$He + NO_2 + OH \rightarrow He + HNO_3$	$2.2\times10^{-30}(300/T_g)^{2.9}$	82
109	$He^* + 2He \rightarrow He_2^* + He$	1.5×10^{-34}	78

T_e in eV, T_g in Kelvin

[a] The rate coefficient is obtained from EEDF using cross sections from indicated reference.

[b] Rate coefficient is in cm^3/s for two-body reactions and cm^6/s for three-body reactions

Reference

[1] Tian L, Nie H, Chatterton N P, Branford-White C J, Qiu Y and Zhu L 2011 *Appl. Surf. Sci.* **257** 7113-8

[2] Gonzalez II E, Barankin M D, Guschl P C and Hicks R F 2010 *Plasma Process. Polym.* **7** 482-93

[3] Furusho H, Kitano K, Hamaguchi S and Nagasaki Y 2009 *Chem. Mater.* **21** 3526-35

[4] Ikawa S, Kitano K and Hamaguchi S 2010 *Plasma Process. Polym.* **7** 33-42

[5] O'connell D, Cox L J, Hyland W B, Mcmahon S J, Reuter S, Graham W G, Gans T and Currell F J 2011 *Appl. Phys. Lett.* **98** 043701

[6] Zhu W C, Li Q, Zhu X M and Pu Y K 2009 *J. Phys. D: Appl. Phys.* **42** 202002

[7] Yonemori S, Nakagawa Y, Ono R and Oda T 2012 *J. Phys. D: Appl. Phys.* **45** 225202

[8] Yuan X, Raja L L. 2002 *Appl. Phys. Lett.* **81** 814-16

[9] Liu D X, Bruggeman P, Iza F, Rong M Z and Kong M G 2010 *Plasma Sources Sci. Technol.* **19** 025018

[10] Liu D X, Rong M Z, Wang X H, Iza F, Kong M G and Bruggeman P 2010 *Plasma Process. Polym.* **7** 846–65

[11] Bourdon A, Darny T, Pechereau F, Pouvesle J-M, Viegas P, Iséni S and Robert E 2016 *Plasma Sources Sci. Technol.* **25** 035002

[12] Tschiersch R, Bogaczyk M and Wagner H E 2014 *J. Phys. D: Appl. Phys.* **47** 365204

[13] Ellerweg D, Benedikt J, von Keudell A, Knake N and Schulz-von der Gathen V 2010 *New J. phys.* **12** 013021

[14] Wang S, Chen Z Y, Wang X H, Li D, Yang A J, Liu D X, Rong M Z, Chen H L and Kong M G 2015 *J. Appl. Phys.* **118** 203301

[15] Massines F, Rabehi A, Decomps P, Gadri R B, Segur P and Mayoux C 1998 *J. Appl. Phys.* **83** 2950-7

[16] Samukawa S *et al* 2012 *J. Phys. D: Appl. Phys.***45** 253001

[17]Breden D, Miki K and Raja L L 2012 *Plasma Sources Sci. Technol.* **21** 034011.

[18] Naidis G V. 2011 *J. Phys. D: Appl. Phys.* **44** 215203.

[19] van Gaens W and Bogaerts A 2013 *J. Phys. D: Appl. Phys.***46** 275201

[20] Murakami T, Niemi K and Gans T 2013 *Plasma Sources Sci. Technol.***22** 015003

[21] Tavant A and Lieberman M A 2016 *J. Phys. D: Appl. Phys.* **49** 465201

[22] Liu D X, Iza F, Wang X H, Kong M G and Rong M Z 2011 *Appl. Phys. Lett.***98** 221501

[23] Vasko C A, Liu D X, Van Veldhuizen E M, Iza F and Bruggeman P J 2014 *Plasma Chem. Plasma Process.* **34** 1081-99

[24] Yang A J, Wang X H, Rong M Z, Liu D X, Iza F and Kong M G 2011 *Phys. Plasmas* **18** 113503

[25] Liu D, Sun B, Iza F, Xu D H, Wang X H, Rong M Z and Kong M G 2017 *Plasma Sources Sci. Technol.* **26** 045009

[26] Sakiyama Y, Graves D B, Chang H W, Shimizu T and Morfill G E 2012 *J. Phys. D: Appl. Phys.* **45** 425201

[27] Dorai R and Kushner M J 2003 *J. Phys. D: Appl. Phys.* **36** 666

[28] Hagelaar G J M and Pitchford L C 2005 *Plasma Sources Sci. Technol.* **14** 722

[29] Kushner M J 1999 *Bull. Am. Phys. Soc.***44** 63

[30] Perin J, Leroy O and Bordage M C 1996 *Contrib. Plasma Phys.* **36** 3

[31] Ding K, Lieberman M A and Lichtenberg A J 2014 *J. Phys. D: Appl. Phys.* **47** 305203

[32] Yang A J, Wang X H, Rong M Z, Liu D X, Iza F and Kong M G 2011 *Phys. Plasmas* **18** 113503

[33] Liu D X, Iza F, Wang X H, Ma Z Z, Rong M Z and Kong M G 2013 *Plasma Sources Sci. Technol.* **22** 055016

[34] Murakami T, Niemi K, Gans T, O'Connell D and Graham W G 2012 *Plasma Sources Sci. Technol.* **22** 015003

[35] Itikawa Y, Ichimura A, Onda K, Sakimoto K, Takayanagi K, Hatano Y, Hayashi M, Nishimura H and TsurubuchiS 1989 *J. Phys. Chem. Ref. Data* **18** 23

[36] Lieberman M A 2015 *Plasma Sources Sci. Technol.* **24** 025009.

[37] Van Gaens W and Bogaerts A 2013 *J. Phys. D: Appl. Phys.* **46** 275201

[38] Malik M A, Ghaffar A and Malik S A 2001 *Plasma Sources Sci. Technol.* **10** 82

[39] Ding K and Lieberman M A 2015 *J. Phys. D: Appl. Phys.***48** 035401

[40] Yang A, Liu D, Rong M, Wang X H and Kong M G 2014 *Phys. Plasmas* **21** 083501

[41] Rauf S and Kushner M J 1999 *J. App. Phys.* **85** 3460

[42] Stalder K R, Vidmar R J, Nersisyan G and Graham W G 2006 *J. Appl. Phys.* **99** 093301

[43] Emmert F, Angermann H H, Dux R and Langhoff H 1988 *J. Phys. D: Appl. Phys.* **21** 667

[44] Quinteros T, Gao H, DeWitt D R, Schuch R, Pajek, M, Asp S and Belki´c D˘z 1995 *Phys. Rev.* A **51** 1340

[45] Stafford D S and Kushner M J 2004 *J. Appl. Phys.* **96** 2451

[46] Kong M G and Deng X T 2003 *IEEE Trans. Plasma Sci.* **31** 7

[47] Golubovskii Yu B, Maiorov V A, Behnke J and Behnke J F 2003 *J. Phys. D: Appl. Phys.* **36** 39

[48] Miller T J, Farquhar P R and Willacy K 1997 *Astrom. Astrophys. Suppl. Ser.* **121** 139

[49] Bortner M H and Baurer T 1972 *Defense Nuclear Agency reaction rate handbook, Final report* (No. AD--763699; DNA--1948-H). General Electric Co., Philadelphia, Pa.(USA).

[50] Deloche R, Monchicourt P, Cheret M, and Lambert F 1976 *Phys. Rev.* A **13** 1140-76

[51] Capitelli M, Ferreira C M, Gordiets B F and Osipov A I 2000 *Plasma Kinetics in Atmospheric Gases* (Berlin: Splinger)

[52] Matzing H 2007 *Adv. Chem. Phys.* **80** 315-402

[53] Kossyi I A, Kostinsky A Yu, Matveyen A A and Silakov V P 1992 *Plasma Sources Sci. Technol.* **1** 207

[54] Kraemer W P, Spirko V and Jurek M 1995 *Chem. Phys. Lett.* **236** 177-83

[55] Ikezoe Y, Matsuoka S, Takebe M and Viggiano A 1987 *Gas Phase Ion-Molecule Reaction Rate Constants Through 1986* (Tokyo: Maruzen)

[56] Albritton D L 1978 *At. Data Nucl. Data Tables* **22** 1

[57] Sakiyama Y and Graves D B 2009 *Plasma Sources Sci. Technol.* **18** 025022

[58] Binns W R and Ahl J L 1978 *J. Chem. Phys.* **68** 538-46

[59] Sanders R A and Muschlitz E E 1977 *Int. J. Mass Sepctro. Ion Phys.* **23** 99-108

[60] Jurek M, Spirko V and Kraemer W P 1995 *Chem. Phys.* **193** 287-96

[61] Eichwald O, Yousfi M, Hennad A and Benabdessadok M D 1997 *J. Appl. Phys.* **82** 4781

[62] Mark T D and Oskam H J 1971 *Phys. Rev.* A **4** 1445

[63] Sommerer T J and Kushner M J 1992 *J. Appl. Phys.* **71** 1654-73

[64] Wynn M J and Martin J D 1970 *J. Chem. Phys.* **52** 191-7

[65] Vidmar R J and Stalder K R 2004 *AFOSR Final Performance Report. (Computations of the power to sustain plasma in air with relevance to aerospace technology. Final report prepared for Air Force Office of Scientific Research.* Report No: AFRISRARRE040123. Contact No. F49620-01-0414. 20 Febraury 2004)

[66] Champion R L, Doverspike L D and Lam S K 1976 *Phys. Rev.* A **13** 617-21

[67] Axford S D T and Hayhurst A N 1996 *Proc. Math. Phys. Eng. Sci.* **452** 1007-33

[68] McDaniel E W, Flannery M R, Thomas E W, Ellis H W, McCann K J, Manson S T, Gallagher J W, Rumble J R, Beaty E C and Roberts T G 1978 *US Army Missile Research and Development Command Technical Report* No H-78-1

[69] Wang Q, Economou D J and Donnelly V M 2006 *J. Appl. Phys.* **100** 023301

[70] Cardoso R P, Belmonte T, Henrion G and Sadeghi N 2006 *J. Phys. D: Appl. Phys.* **39** 4178-85

[71] Hagelaar G J M and Kroesen G M W 2000 *J. Appl. Phys.* **88** 5

[72] Adams N G, Bohme D K and Ferguson E E 1970 *J. Chem. Phys.* **52** 5101-5

[73] Ivanov V A and Skoblo Yu E 2005 *Opt. Spectrosc.* **98** 811–818

[74] Shibata T, Fu8kuyama T and Kuchitsu K 1973 *J. Mass Spectrom. Soc. Jpn.* **21** 217-21

[75] Takao S, Kogoma M, Oka T, Imamura M and Arai S 1980 *J. Chem. Phys.* **73** 148-55

[76] Ricard A, Decomps Ph and Massines F 1999 *Surf. Coat. Technol.* **112** 1-4

[77] Martens T, Bogaerts A, Brok W J M and Dijk J V 2008 *Appl. Phys. Lett.* **92** 041504

[78] Niemi K, Waskoenig J, Sadeghi N, Gans T and O'Connell D 2011 *Plasma Sources Sci. Technol.* **20** 055005

[79] Castillo M, M'endez I, Islyaikin A M, Herrero V J and Tanarro I 2005 *J. Phys. Chem.* A **109** 6255

[80] Tsang W and Hampson R F 1986 *J. Phys. Chem. Ref. Data* **15** 1087-222

[81] GRI-MECH 3 Reaction Rate Database. http://www.me.berkeley.edu/gri-mech/

[82] Herron J T and Green D S 2001 *Plasma Chem. Plasma Process.* **21** 459

[83] Atkinson R, Baulch D L, Cox R A, Hampson R F, Kerr J A, Rossi M J and Troe J 1997 *J. Phys. Chem. Ref. Data* **26** 1329

[84] National Institute of Standards and Technology, cited 2011: *NIST Chemical Kinetics Database* (Available online at http://kinetics.nist.gov/)

[85] Person J C and Ham D O 1988 *Int. J. Radiat. Appl. Instrum.* Part C **31** 1

[86] Henry R, Burke P and Sinfailam A L 1969 *Phys. Rev.* **178** 218-25

[87] Malone C P, Johnson P V, Liu X, Ajdari B, Kanik I and Khakoo M A 2012 *Phys. Rev.* A **85** 062704

[88] Laher R R and Gilmore F R 1990 *J. Phys. Chem. Ref. Data* **19** 277-305

[89] Eliasson B and Kogelschatz U 1986 *Basic data for modelling of electrical discharges in gases: oxygen*(ABB Asea Brown Boveri).

[90] Yousfi M and Benabdessadok M D 1996 *J. Appl. Phys.* **80** 6619

[91] Itikawa Y and Mason N 2005 *J. Phys. Chem. Ref. Data* **34** 1-22

[92] Samiolovich V G, Popovich M P, Emelyanov Yu M and Filippov Yu V 1966 *J. Phys. Chem.***40** 287

[93] Rapp D and Briglia D D 1965 *J. Chem. Phys.* **43** 1480-9

[94] McConkey J W, Malone C P, Johnson P V, Winstead C, Mckoy V and Kanik 2008 *Phys. Rep.* **466** 1-103

[95] McConkey J W, Malone C P, Johnson P V, Winstead C, McKoy V and Kanik I 2008 *Phys. Rep.***466** 1

[96] Itikawa Y and Mason N 2005 *J. Phys. Chem. Ref. Data***34** 1-22

[97] Matzing H 2007 *Adv. Chem. Phys.* **80** 315–402

[98] Sieck L W, Herron J T and Green D S 2000 *Plasma Chem. Plasma Process.* **20** 235

[99] Anicich V G 1993 *J. Phys. Chem. Ref. Data* **22** 1469

[100] Olson R E, Peterson J R and Moseley J T 1970 *J. Chem. Phys.* **53** 3391

[101] Bortner M H and Baurer T 1979 *Defense Nuclear Agency Reaction Rate Handbook* Second Edition, Section 24 Revision No 7, NTIS AD-763699

[102] Cenian A, Chernukho A and Borodin V 1995 *Contrib. Plasma Phys.* **35** 273

[103] Tochikubo F and Arai H 2002 *Japan. J. Appl. Phys.* **41** 844

[104] Kushner M J 1993 *J. Appl. Phys.* **74** 6538